

High-temperature superconductivity in iron pnictides and chalcogenides

Qimiao Si¹, Rong Yu^{2,3} and Elihu Abrahams⁴

Abstract | Superconductivity develops in metals upon the formation of a coherent macroscopic quantum state of electron pairs. Iron pnictides and chalcogenides are materials that have high superconducting transition temperatures. In this Review, we describe the advances in the field that have led to higher superconducting transition temperatures in iron-based superconductors and the wide range of materials that are used to form these superconductors. We summarize the essential aspects of the normal state and the mechanism for superconductivity. We emphasize the degree of electron–electron correlations and their manifestation in properties of the normal state. We examine the nature of magnetism, analyse its role in driving the electronic nematicity and discuss quantum criticality at the border of magnetism in the phase diagram. Finally, we review the amplitude and structure of the superconducting pairing, and survey the potential material settings for optimizing superconductivity.

In 2008, the discovery¹ of superconductivity in an iron pnictide with a critical temperature for the superconducting transition (T_c) of 26 K took the condensed-matter community by surprise. It raised the prospect of finding high-temperature superconductivity in compounds other than copper-based materials — the only known materials at the time with $T_c > 40$ K (REF. 2). Although an increased T_c of 56 K in iron pnictides was reported after only a few months³, this new record remained unbroken for several years. Recent developments in the study of iron chalcogenides^{4–8}, however, have renewed hope of reaching a higher T_c . In the meantime, considerable progress has been made towards the understanding of the microscopic physics of these iron-based superconductors (FeSCs).

In FeSCs, superconductivity pairing does not arise from the conventional electron–phonon coupling⁹; instead, it is a consequence of an unconventional pairing mechanism generated by the electron–electron Coulomb interaction. Qualitatively, electrons form pairs under the action of an attractive force that is generated while their mutual Coulomb repulsion is avoided (BOX 1).

Two important characteristics of FeSCs provide an indication of the mechanism behind their unconventional superconductivity: first, in the phase diagram, superconductivity emerges out of a ‘bad-metal’ normal state; second, the superconducting phase occurs near the onset of antiferromagnetic (AFM) order. Unconventional superconductivity has led to extensive experimental and theoretical studies on the effect of electron correlations and on the nature of magnetism in iron pnictides and

chalcogenides, and, hence, to the discovery of several notable properties. These include the quantum criticality that arises at the border of AFM order as well as the electronic nematicity — the lowering of lattice rotational symmetry — and its relationship with magnetism. All these effects are closely connected to the amplitude and structure of the superconducting pairing.

In this Review, we summarize the range of materials available for use in FeSCs and their electronic structures; we then discuss key aspects of their microscopic physics. At present, various theoretical approaches are being used to understand these systems. Rather than describing theoretical frameworks, we organize the discussion by taking into consideration the hierarchy of the relevant energy scales: we first discuss the Coulomb repulsion (about 1 eV), followed by antiferromagnetism (about 0.1 eV) and, finally, superconductivity, for which the pairing energy scale is about 0.01 eV. The conclusions include a survey of the prospects for further discoveries and understanding, as well as of the implications that studies of FeSCs have for the general field of unconventional superconductivity.

Materials and electronic structures

The structures of several iron pnictides and chalcogenides are shown in FIG. 1a. A common feature of these materials is the presence of either iron–pnictogen or iron–chalcogen trilayers. In each FeAs/FeSe trilayer, the iron ions form a square lattice, and the arsenic or selenium ions are located above or below the centre of a square of iron ions. LaFeAsO belongs to the 1111

¹Department of Physics and Astronomy, Rice University, Houston, Texas 77005, USA.

²Department of Physics and Beijing Key Laboratory of Opto-electronic Functional Materials and Micro-nano Devices, Renmin University, Beijing 100872, China.

³Department of Physics and Astronomy, Collaborative Innovation Center of Advanced Microstructures, Shanghai Jiaotong University, Shanghai 200240, China.

⁴Department of Physics and Astronomy, University of California Los Angeles, Los Angeles, California 90095, USA.

qmsi@rice.edu;

rong.yu@ruc.edu.cn;

abrahams@physics.ucla.edu

Article number: 16017

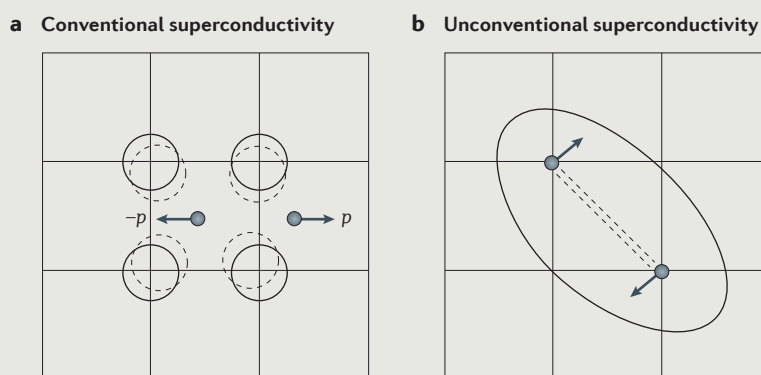
doi:10.1038/natrevmats.2016.17

Published online 11 Mar 2016

Box 1 | History and basics of superconductivity

Superconductivity was discovered by H. Kamerlingh Onnes more than a century ago¹⁴⁴ and the phenomenon was explained by Bardeen, Cooper and Schrieffer (BCS) in a remarkable paper¹⁴⁵ in 1957. Superconductivity develops when electron pairs with opposite momenta in a crystal condense into a coherent state, that is, when the electrons in each pair move in unison and conduct electricity without experiencing any resistive loss of energy. In BCS theory, which describes conventional superconductors, electrons form pairs through an attractive interaction that is mediated by phonons, the quantized ionic vibrations. As depicted in the figure (panel a), the passage of the first electron leaves a distortion in the lattice formed by the ions, which attracts a second electron with opposite momentum, p . Concurrently, Coulomb repulsion is avoided, because a pair is formed between electrons separated by a time delay.

In unconventional superconductivity, electron pairs are formed through attractive interactions that are generated while avoiding Coulomb repulsion through the spatial anisotropy in the relative motion of the electrons (panel b). Pairing correlations will be unfavourable between electrons on the same site, which experience the dominant repulsive interactions. Instead, pairing correlations develop between electrons from different sites. As a consequence, the orbital part of the pairing wave function tends to be in channels that are orthogonal to the conventional s -wave channel; these channels range from extended s waves to cases with angular momentum larger than zero.



iron-pnictide family and comprises FeAs trilayers that are separated by LaO layers. The maximum T_C (56 K) in this family has been achieved in the SmFeAsO system with fluorine doping³. BaFe_2As_2 is a member of the 122 iron-pnictide family¹⁰; each unit cell contains two FeAs trilayers separated by a layer of barium ions. In this class of materials, superconductivity arises following chemical substitution into the undoped compound, as illustrated in FIG. 1b for the case of Ni_x substitution into BaFe_2As_2 . The maximum T_C that has been reached in 122 iron pnictides is 38 K in $\text{Ba}_{0.6}\text{K}_{0.4}\text{Fe}_2\text{As}_2$. As for iron chalcogenides, FeSe has the simplest structure in this category¹¹, with each unit cell consisting of an FeSe trilayer. Each FeSe trilayer corresponds to a selenium-for-arsenic replacement of an FeAs trilayer. The potassium iron selenides^{12,13}, $\text{K}_x\text{Fe}_{2-y}\text{Se}_2$, can be viewed as derived from the FeSe system by inserting potassium ions between two FeSe trilayers. In these bulk iron selenides, the maximum T_C that has been reached is 31 K — comparable to that of the 122 iron pnictides.

Recently, ‘single-layer’ FeSe on a SrTiO_3 substrate has been fabricated^{4,6}. In this system, there is substantial evidence for superconductivity up to 65 K, as indicated by the opening of a gap in the electron spectrum⁵ and by the onset of the Meissner effect⁷; a T_C of 109 K has been reported from electrical transport measurements⁸.

Despite the similarities in their crystal structures, an important feature of FeSCs is a large variability in their electronic structures, which can be appreciated by looking at their Fermi surfaces (FIG. 1c). The typical Fermi surfaces of iron pnictides comprise hole Fermi pockets in the middle of the Brillouin zone and electron Fermi pockets at the boundaries¹⁴. By contrast, in several iron chalcogenides there are only electron Fermi pockets, as in the case of single-layer FeSe on a SrTiO_3 substrate and of $\text{K}_x\text{Fe}_{2-y}\text{Se}_2$. This last system, however, contains an additional electron pocket near the Γ point in the Brillouin zone, as discussed later. To cite another example, in a class of extremely hole-doped FeSCs, such as KFe_2As_2 , the zone-boundary electron-like Fermi surfaces are absent, having turned into tiny hole Fermi pockets after a Lifshitz transition¹⁵. We note that FIG. 1c shows the Fermi surfaces in the purely 2D Brillouin zone of the one-iron unit cell. In reality, they are quasi-2D and ‘warp’ (disperse) along the third direction of the wave-vector space, to a different degree depending on the material.

Correlations and bad-metal behaviour

The microscopic physics of FeSCs can be better understood by considering the observation that the metallic phases of FeSCs are all characterized by bad-metal properties. Experimental and theoretical studies of such bad-metal behaviour have provided considerable insight into the degree of electron correlations in these materials.

Iron pnictides and chalcogenides as bad metals. Consider a representative iron arsenide, such as BaFe_2As_2 . It is metallic and develops AFM order at a Néel temperature (T_N) of roughly 140 K (REF. 16). Similar to the other iron-based compounds, above the T_N it is a paramagnetic metal with a rather large electrical resistivity. Several iron compounds are sufficiently clean to enable the observation of quantum oscillations at low temperature; however, they all have a very large electrical resistivity at room temperature. This property defines a bad metal by the Mott–Ioffe–Regel criterion¹⁷: the mean free path, ℓ , is very short, of the order of interparticle spacing, and its product with the magnitude of the Fermi wave vector, k_F , is of the order of unity. To estimate $k_F\ell$, we can start from the observation that the number of bands crossing the Fermi level, p , is usually 4 or 5 (FIG. 1c). Based on the typical magnitude of the single-crystal in-plane resistivity at room temperature (about $400\ \mu\Omega\text{ cm}$), the estimated $k_F\ell$ is approximately $5/p \approx 1$ for each Fermi pocket¹⁸. This value should be contrasted with the corresponding value for a good metal, such as chromium, for which the resistivity in the paramagnetic state just above room temperature is about 40 times smaller¹⁹.

Because electron–phonon scattering gives a much smaller contribution to the resistivity (typically several $\mu\Omega\text{ cm}$), such a small value of $k_F\ell$ in iron pnictides implies strong electron–electron interactions^{20,21}.

Another signature of the strong electronic correlations in these systems is the considerable reduction in the weight of the Drude peak in the optical conductivity; the spectral weight of this peak is about 30% of the

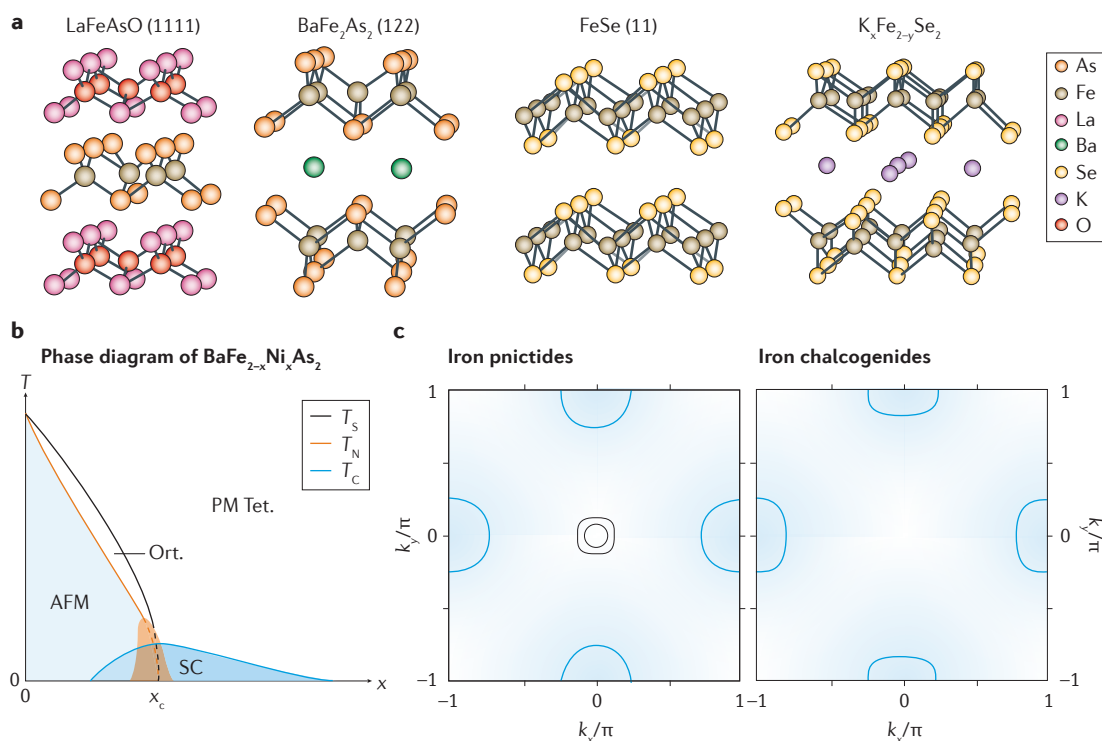


Figure 1 | Materials characteristics of iron-based superconductors. **a** | Crystal structure of LaFeAsO (1111), BaFe₂As₂ (122), FeSe (11) and K_xFe_{2-y}Se₂. **b** | Schematic phase diagram of BaFe_{2-x}Ni_xAs₂ in the temperature T and chemical-substitution x plane. **c** | Schematic Fermi surfaces of iron pnictides and of several iron chalcogenides, showing the electron pockets in blue and the hole pockets in grey. AFM, antiferromagnetic; $k_{x/y}$, components of the wave vector for single-particle excitations in the x and y direction, respectively; Ort., orthorhombic; PM Tet., paramagnetic tetragonal; SC, superconducting; T_C , superconducting transition temperature; T_N , Néel temperature; T_S , structural transition temperature; x_c , critical doping for the quantum critical point. Panel **a** is adapted with permission from REF. 1, American Chemical Society; REF. 11, copyright (2008) National Academy of Sciences, U.S.A; and REF. 146, Elsevier. Panel **b** is adapted with permission from REF. 114, American Physical Society. Panel **c** is from REF. 49, Nature Publishing Group.

value expected from non-interacting electrons²² (FIG. 2a). This reduction is sizable, of the same order as that observed in other bad metals, such as the normal state of the doped cuprate superconductors and of V₂O₃, for which correlation effects are of primary importance. A corollary is that about 70% of the spectral weight resides in an incoherent part of the spectrum, associated with electronic states away from the Fermi energy. Similar behaviour has been reported in various iron pnictides²³.

The reduction in the weight of the Drude peak is accompanied by the mass renormalization observed in angle-resolved photoemission spectroscopy (ARPES). In iron arsenides, the ratio of the observed effective mass of the electron in the paramagnetic phase to the band mass (m^*/m_b) is roughly 3–4 (REFS 14, 24), which indicates the importance of the correlation-induced mass enhancement. In iron chalcogenides, which are also bad metals with the room-temperature resistivity reaching the Mott–Ioffe–Regel limit, the correlation-induced mass enhancement is even larger — as large as 20 for some of the involved bands^{25–27}.

These bad-metal properties suggest that the electron–electron correlations are sufficiently strong to place the metallic iron pnictides and chalcogenides in the proximity of a Mott localization. Thus, the question arises of

whether it is possible to tune the strength of the electron correlations to push these and related materials into the Mott insulating state.

Mott insulators in iron chalcogenides. A measure of the strength of the electron correlations is given by the ratio of the local electron–electron interaction to the electron bandwidth or the kinetic energy. Therefore, reducing the kinetic energy would effectively enhance correlation effects. This stimulated interest in iron oxychalcogenides, La₂O₂Fe₂O(Se, S)₂. Similar to the FeAs trilayer of the iron pnictides, each Fe₂O(Se, S)₂ layer contains a square lattice of iron ions, which also have a nominal valency of +2. However, the iron–iron distance is bigger, leading to a reduced kinetic energy. Electronic-structure calculations demonstrated that the iron 3d-electron bandwidth is about 75% of that found in the usual compounds, such as LaFeAsO and BaFe₂As₂; the enhanced electron correlation effects highlight the possibility of observing a Mott insulating state in these materials²⁸. Experimentally, their insulating nature is demonstrated by the temperature dependence of the electrical resistivity (FIG. 2b), which shows an activated behaviour with moderate charge gaps (0.19 eV and 0.24 eV for the selenium and sulfur cases, respectively). AFM ordering

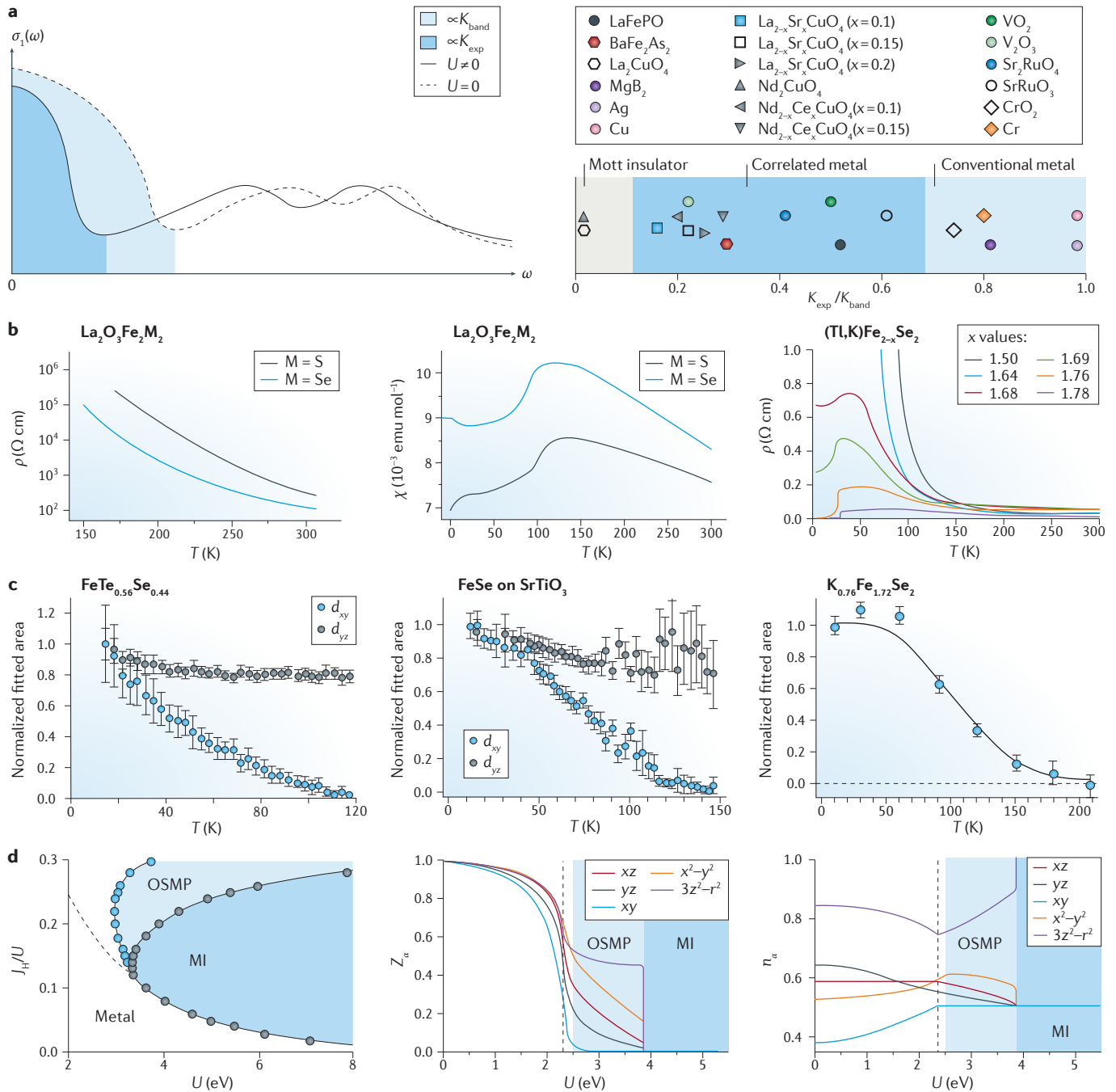


Figure 2 | Bad-metal behaviour and electron correlations. **a** | Left, gauging electron correlations from the ratio of K_{exp} , the measured Drude weight of the optical conductivity, $\sigma_1(\omega)$, as a function of frequency, ω , to K_{band} , its non-interacting counterpart. The solid and the dashed lines correspond to a non-zero and zero value of the Hubbard interaction, U , respectively. Shaded regions represented are proportional to K_{exp} and K_{band} . Right, $K_{\text{exp}}/K_{\text{band}}$ for various systems, including the iron arsenides. **b** | Insulating iron chalcogenides. Resistivity, ρ , (left) and magnetic susceptibility, χ , (middle) as a function of temperature, T , for the oxychalcogenides. Right, ρ as a function of T for the alkaline iron selenides, with different dopings x as indicated. **c** | Quasi-particle weight near the Fermi level determined from angle-resolved photoemission spectroscopy data for bands with distinct xy and yz characters, providing evidence for the orbital-selective Mott phase (OSMP) in $\text{FeTe}_{0.56}\text{Se}_{0.44}$ (left), monolayer FeSe film on SrTiO_3 (middle) and $\text{K}_{0.76}\text{Fe}_{1.72}\text{Se}_2$ (right). The normalized fitted area is the fitted area of the d_{xy}

and d_{yz} peaks, normalized by the initial value of the peak area. d_{xy} and d_{yz} are the 3d xy and yz orbitals. **d** | Left, ground-state phase diagram for alkaline iron selenides at $N=6$. The dark and light blue regions correspond to the Mott insulator (MI) phase and OSMP, respectively. The black dashed line indicates a crossover into a strongly correlated metal regime. Middle, in the OSMP, the quasi-particle weight, Z_a , vanishes for the 3d xy orbital but is non-zero for the others (indicated in the legend). Right, several orbitals are already close to half-filling ($n_a \approx 0.5$) for moderate strengths of the interaction parameter. J_H , Hund's coupling. Panel **a** (left) is from REF. 147, Nature Publishing Group. Panel **a** (right) is from REF. 22, Nature Publishing Group. Panel **b** (left and middle) is adapted with permission from REF. 28, copyright (2010) by the American Physical Society. Panel **b** (right) is adapted with permission from REF. 32, Institute of Physics. Panel **c** is from REF. 27, Nature Publishing Group. Panel **d** is adapted with permission from REF. 41, American Physical Society.

occurs around a T_N of roughly 93 K and 105 K for the selenium and sulfur cases, respectively, as indicated by the temperature dependence of the magnetic susceptibility (FIG. 2b) and by neutron-scattering studies²⁹. The insulating behaviour persists above the T_N , a characteristic signature of a Mott insulator³⁰. Finally, the incoherent electronic excitations of this correlated insulating state have recently been observed by X-ray spectroscopy³¹.

Insulating behaviour has been observed in several other iron chalcogenides. One example is the alkaline iron selenides³² (FIG. 2b). They have a 245 composition, $A_{0.8}Fe_{1.6}Se_2$ ($A=K, Tl/K$ or Rb), in which one out of the five iron atoms is absent in each FeSe trilayer³³. It has been suggested that the ordered vacancies reduce the kinetic energy and, similar to the case of the oxychalcogenides described above, give rise to a Mott insulating state^{34,35}. The alkaline iron selenides also have a 234 phase, $AFe_{1.5}Se_2$, for which the Mott insulator nature has been suggested as well, on the basis of ARPES measurements³⁶.

Orbital-selective Mott physics. To study the effect of electron correlations, it is important to acknowledge the multi-orbital nature of the electronic states. Conversely, the multi-orbital physics can be used to extract information about the degree and nature of the electron correlations. $BaFe_2As_2$ is an example of a parent compound (that is, undoped), in which the iron valency is +2. In these compounds, there are on average $N=6$ electrons that occupy the five $3d$ orbitals of each iron ion. The theoretical description is given by multi-orbital Hubbard models, with the minimal interactions being a Hubbard interaction (direct Coulomb repulsion), U , and a Hund's coupling, J_H . Such models typically include at least the $3d$ xy and xz/yz orbitals, and can include all five $3d$ orbitals. The interplay among the kinetic energy, U and J_H can lead to different behaviour for the various orbitals. It might even be possible that a subset of these orbitals undergoes Mott localization, that is, orbital-selective Mott physics. ARPES measurements have provided evidence^{26,27} for an orbital-selective Mott phase (OSMP). These measurements (FIG. 2c) show that, for each of the three considered iron chalcogenides, as temperature increases above about 100 K, the spectral weight for the $3d$ xy orbital vanishes, whereas for the $3d$ xz/yz orbitals it does not change substantially. The experimental results suggest that this regime can be described by an OSMP, in which the $3d$ xy electrons are localized, whereas those associated with the other $3d$ orbitals remain itinerant. Additional evidence for the OSMP has come from THz spectroscopy³⁷, Hall measurements³⁸, pump-probe spectroscopy³⁹ and high-pressure transport measurements⁴⁰.

The OSMP was anticipated theoretically. FIGURE 2d shows the zero-temperature phase diagram calculated for potassium iron chalcogenides at the $3d$ -electron filling $N=6$, in the paramagnetic case with tetragonal lattice symmetry (the paramagnetic case is used instead of the AFM-ordered one to highlight the localization effects associated with the Coulomb repulsive interactions). When the U and J_H interactions are sufficiently large, a Mott insulating phase arises. An OSMP appears between

this phase and that in which all the $3d$ orbitals are itinerant^{41,42}. When the electron filling deviates from the commensurate value $N=6$, the Mott insulator phase is suppressed, but the OSMP is observed for a finite range of electron filling. Similar results arise from a model without the ordered iron vacancies⁴¹. If at a temperature of zero the system is purely itinerant, but close to the boundary of the OSMP, then increasing the temperature induces a crossover to the OSMP, which is consistent with experimental observations (FIG. 2c).

Several factors are responsible for the OSMP. First, in the non-interacting limit, the bandwidth of the xy orbital is smaller than that of the other orbitals. Second, the J_H suppresses inter-orbital correlations; this effectively decouples the $3d$ xy orbital from the others and keeps the xy , xz and yz orbitals effectively half-filled — such an inter-orbital decoupling is essential for the stability of the OSMP, given that the orbitals are mixed in the non-interacting limit. Third, the degeneracy of the xz and yz orbitals makes the interaction threshold for their localization higher than its counterpart for the non-degenerate xy orbital⁴³. As a combined effect of these factors, the $3d$ xy orbital has a lower interaction threshold for the Mott transition, and the OSMP arises. The OSMP is an extreme limit of the effect of orbital-selective correlations. More generally, the $3d$ xy orbital is not Mott localized but is close to a Mott localization, and the system can still exhibit strong orbital-dependent effects^{44–46}. The OSMP is also observed in other classes of strongly correlated electron systems^{43,47}.

The experimental observations and general considerations summarized in this section highlight the importance of electron–electron correlations in determining the properties of iron pnictides and chalcogenides. They provide the basis for ‘strong coupling’ approaches to the study of these systems^{20,44–46,48–60}, in which the effect of electron–electron interactions is treated non-perturbatively.

Magnetism and electronic nematicity

Magnetism has received considerable attention⁶¹, because AFM order typically exists near superconductivity in the phase diagram. There has also been increasing interest in the role that nematic order — the breaking of orientational symmetry — can play in uncovering the microscopic physics of these systems.

Magnetism in iron pnictides. The parent iron pnictides are antiferromagnetically ordered (FIG. 1b). The ordering wave vector is $(\pi, 0)$ — the notation is that of the iron square lattice (FIG. 3a). This AFM order is the background for the quantum fluctuations of the spins below the T_N . These quantum fluctuations have been probed by inelastic neutron scattering¹⁶, which measures the frequency, ω , and wave-vector, \mathbf{q} , dependence of the spin structure factor, $S(\mathbf{q}, \omega)$, and of the imaginary part of the dynamical spin susceptibility, $\chi''(\mathbf{q}, \omega)$.

A striking feature is that the spin fluctuations remain very strong over a wide temperature range above the T_N (REFS 62–64). In FIG. 3a, the dynamical spin structure factor is shown in terms of equal-intensity contours in

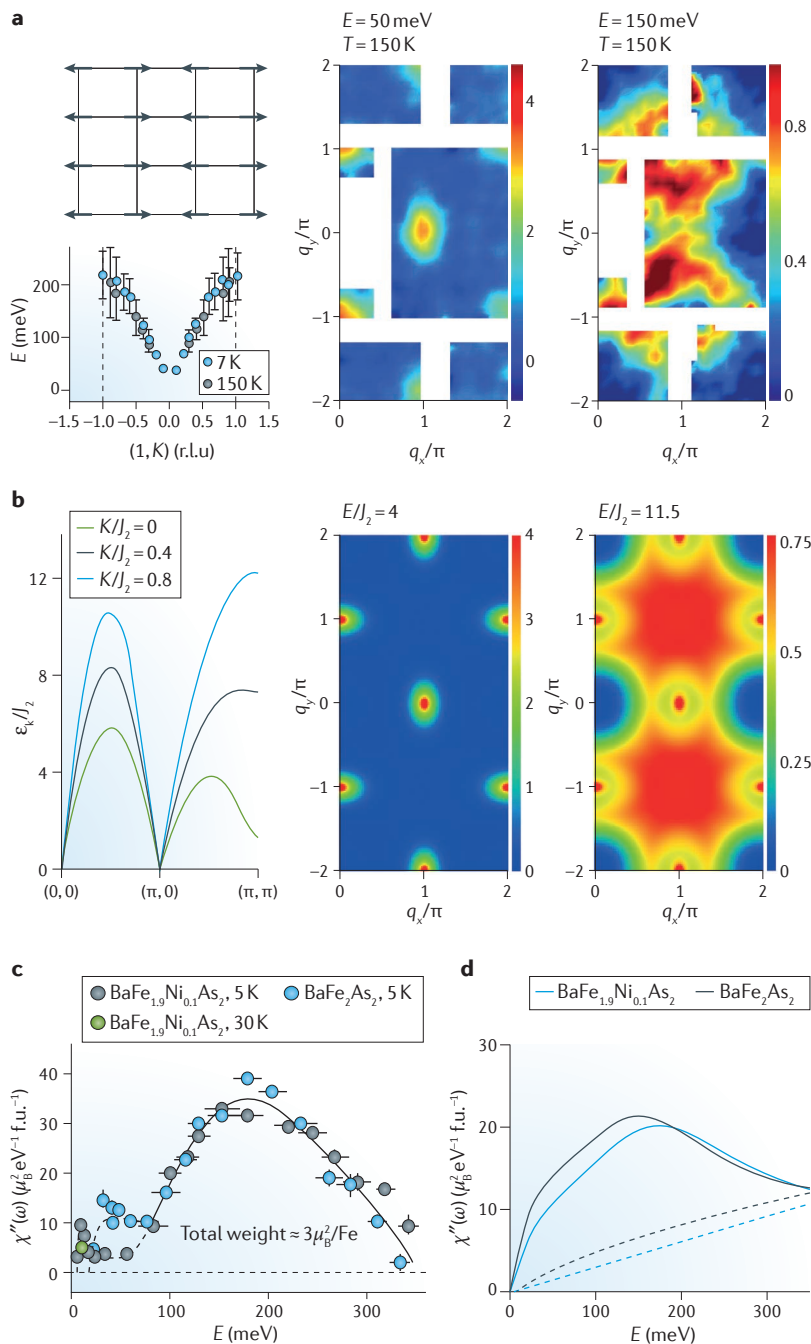


Figure 3 | Magnetism in the iron pnictides. **a** | The magnetic ordering pattern of the parent iron pnictides such as BaFe_2As_2 (top left). The energy dispersion, E , versus wavevector along a cut in the Brillouin zone specified by $(1, K)$ in reciprocal lattice units (r.l.u.) (bottom left) and spin structure factor (colour scales; middle and right) measured in BaFe_2As_2 above the Néel temperature. **b** | Theoretically calculated energy dispersion, ϵ_k/J_2 , (left) and spin structure factor (colour scales; middle and right) within a J_1 - J_2 - K model, where J_1 and J_2 are the exchange interactions between the nearest-neighbour and next-nearest-neighbour sites, respectively. **c** | Imaginary part of the dynamical local spin susceptibility, χ'' , measured in pure and Ni-doped BaFe_2As_2 , versus energy, $E = \hbar\omega$. **d** | The same quantity as in panel **c**, but calculated from dynamical mean-field theory with strong correlations (solid lines) and from the weak-coupling random-phase approximation method (dashed lines). μ_B , Bohr magneton; f.u., formula unit; $q_{x/y}$, components of the wave vector for magnetic excitations in the x and y direction, respectively; ω , frequency. Panel **a** is adapted with permission from REF. 63, American Physical Society. Panel **b** is adapted with permission from REF. 69, copyright (2012) by the American Physical Society. Panels **c** and **d** are from REF. 71, Nature Publishing Group.

wave-vector space at two different energies, $E = \hbar\omega$. At relatively low energies, these are ellipses near $(\pm\pi, 0)$ and $(0, \pm\pi)$. At high energies, they have the form of spin-wave-like excitations reaching the boundaries of the AFM Brillouin zone⁶³. The peak intensity exhibits a spin-wave-like energy dispersion (FIG. 3a).

The electron correlation effects implied by the bad-metal behaviour discussed before have inspired the study of magnetism using local moments as a starting point. Electron correlations turn the majority of the single-electron excitations incoherent and distribute them away from the Fermi energy. In this approach to the study of magnetism, an expansion was developed in terms of the fraction, w , of the single-electron spectral weight that lies in the low-energy coherent part of the spectrum^{20,21}. To zeroth order in w , the incoherent electronic excitations (if their charge degrees of freedom are ‘integrated out’) give rise to localized magnetic moments associated with the iron ions. In the case of iron arsenides, the p orbitals of the arsenic ions mediate the exchange interactions among the local moments. This leads to geometrical frustration of magnetism: because each arsenic ion sits at an equal distance from the iron ions of a square plaquette in the square lattice (FIG. 1a), the exchange interaction is sizeable not only between the nearest-neighbour sites (J_1) on the iron square lattice, but also between the next-nearest-neighbour sites (J_2)^{20,65,66}. General considerations suggest that $J_2 > J_1/2$ (REF. 20). In this parameter regime, the ground state of the J_1 - J_2 Heisenberg model of the square lattice has the collinear $(\pi, 0)$ order⁶⁷, as observed experimentally⁶¹. Because the charge gap in the incoherent excitations is relatively small, and owing to the J_H in the multi-orbital setting of the iron-based compounds⁶⁸, multiple spin couplings can be important. In particular, the four-spin biquadratic coupling, K , of the form $K(\mathbf{S}_i \cdot \mathbf{S}_j)^2$, in which \mathbf{S}_i and \mathbf{S}_j are the spins of electrons at two different sites, i and j , was shown to be relevant^{69,70}. Moreover, at a higher order in w , there are itinerant coherent electrons that are coupled to the local moments and that introduce damping to the spin excitations. The calculated spin structure factor⁶⁹ for the J_1 - J_2 - K model in the presence of damping is displayed in FIG. 3b, also at two different energies. The theoretical results provide a consistent understanding of the experimental data.

Because the majority of the electron spectral weight is in the incoherent sector, the above discussion implies that the spin spectral weight is large. This hypothesis can be tested experimentally. In FIG. 3c, χ'' — the momentum-integrated dynamical spin susceptibility⁷¹ — is shown as a function of energy, E . A further integration over energy (corresponding to $\int dE \int d\mathbf{q} \chi''(\mathbf{q}, E)$) yields a total spectral weight of about $3\mu_B^2$ per iron ion (μ_B is the Bohr magneton). This is equivalent to the spin spectral weight of a full spin-1/2 moment, which corresponds to $1\mu_B$ per iron ion, as anticipated.

The spin spectral weight and its energy distribution provide another way to characterize the strength of electron correlations. For weak correlations, the spin degrees of freedom should be described in terms

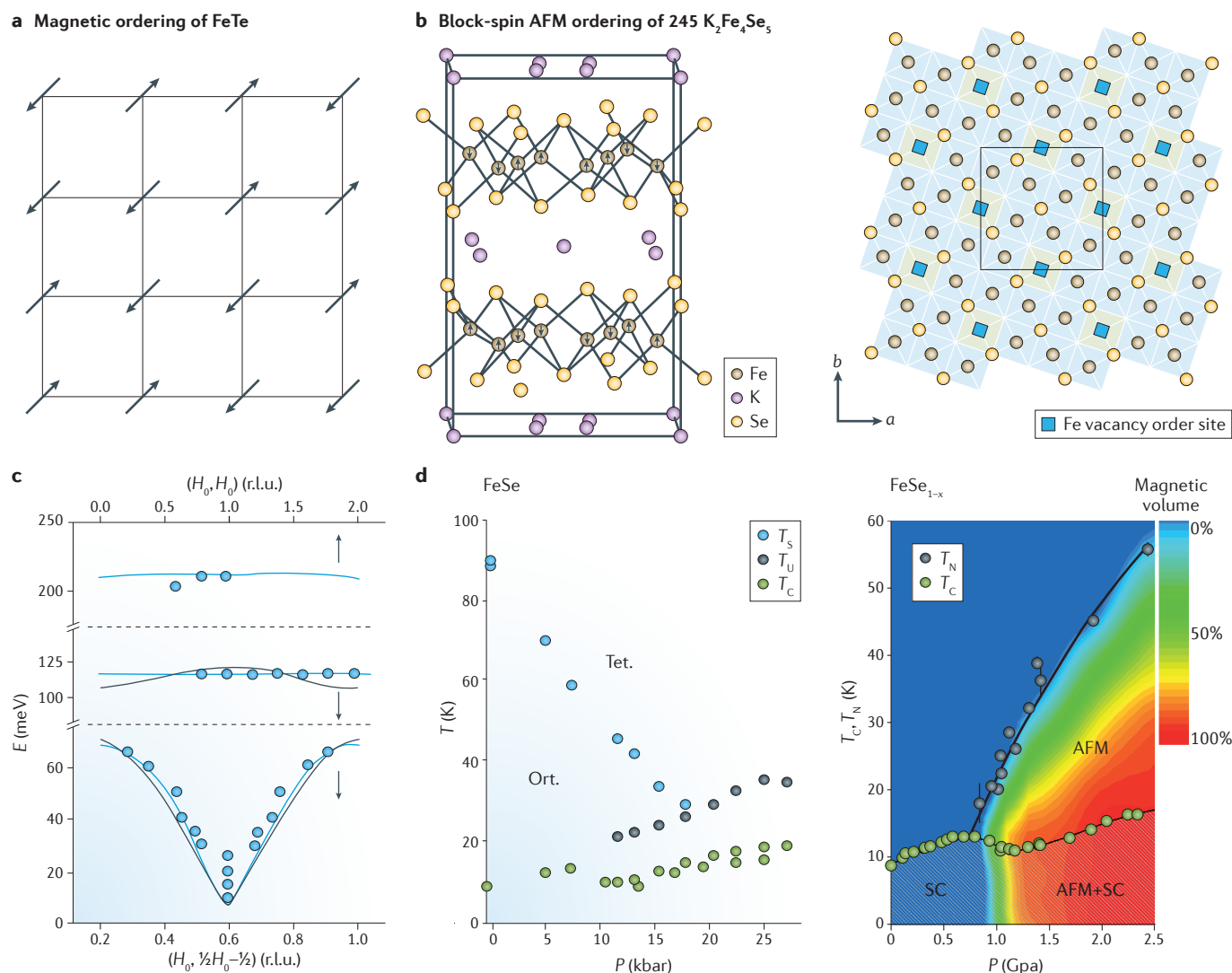


Figure 4 | Magnetism in iron chalcogenides. **a** | The magnetic ordering pattern of FeTe. **b** | The block-spin antiferromagnetic (AFM) order in the $245\text{ K}_2\text{Fe}_4\text{Se}_5$. **c** | The corresponding spin-wave dispersion, E versus wavevector, along two cuts of the Brillouin zone; one cut corresponds to $(H_0, \frac{1}{2}H_0 - \frac{1}{2})$ and the other to (H_0, H_0) , both in reciprocal lattice units (r.l.u.). **d** | Phase diagram of bulk FeSe, showing the structural transition and pressure-induced superconductivity (left) and the pressure-induced magnetic order (right). Ort., orthorhombic; P , pressure; SC, superconducting; T , temperature; T_C , superconducting transition temperature; Tet., tetragonal; T_S , structural transition temperature; T_U and T_N , Néel temperature extracted from resistivity and magnetic measurements, respectively. Panel **b** is adapted with permission from REF. 33, Institute of Physics. Panel **c** is from REF. 78, Nature Publishing Group. Panel **d** (left) is adapted with permission from REF. 148, Physical Society of Japan. Panel **d** (right) is adapted with permission from REF. 149, American Physical Society.

of triplet excitations of electrons and holes near the Fermi energy. In such a weak-coupling description^{72,73}, the enhancement of the spin excitations near $(\pm\pi, 0)$ and $(0, \pm\pi)$ would arise from a Fermi surface ‘nesting’ effect — the enhanced phase space for connecting the electron and hole Fermi pockets near these wave vectors. However, the small size of the electron and hole Fermi pockets would limit their contributions to the spin spectral weight to a value that is considerably smaller than that observed using the integrated dynamical susceptibility.

A quantitative analysis is shown in FIG. 3d. Calculations based on dynamical mean-field theory (solid lines), which incorporate the contributions of the incoherent

part of the electron spectral weight, capture the right size of the spin spectral weight within the energy range of experimental measurements⁷⁴. By contrast, a weak-coupling calculation based on the random-phase approximation (dashed lines) considerably underestimates the spin spectral weight.

Magnetism in iron chalcogenides. AFM order appears in various iron chalcogenides. In FeTe it forms the pattern illustrated in FIG. 4a, corresponding to an ordering wave vector $(\pi/2, \pi/2)$. This ordering pattern can be understood in terms of local moments coupled through multi-neighbour J_1 – J_2 – J_3 exchange interactions in the presence of the biquadratic K couplings^{59,74}. In this case,

the spin spectral weight, $\int dE \int d\mathbf{q} \chi''(\mathbf{q}, E)$, is even larger than the one discussed before, given that the ordered moment is already $2.5\mu_B$ per iron ion⁷⁵.

These observations further elucidate the underlying microscopic physics. The Fermi surface in the paramagnetic state of 11 iron chalcogenides (that is, FeTe) is similar to that of iron pnictides, as seen in FIG. 1c. For these Fermi surfaces $(\pi/2, \pi/2)$ is not a nesting wave vector. Therefore, the magnetic ordering pattern in FeTe cannot be understood within an itinerant nesting description. This suggests that the above considerations on the spin spectral weight of iron pnictides also apply to the FeTe case.

The 245 alkaline iron selenides (for example, $K_2Fe_4Se_5$) have a block-spin AFM order (FIG. 4b). In this case the ordered moment is also large, about $3.3\mu_B$ per iron ion. This magnetic order can be understood in terms of an extended J_1 – J_2 model on a $1/5$ -depleted square lattice with a $\sqrt{5} \times \sqrt{5}$ vacancy order^{76,77}. The four branches of the observed spin-wave spectra, along with a theoretical fit based on the local-moment model, are displayed in FIG. 4c. The good agreement between the experimental data and this local-moment description of the magnetic dynamics, together with the large ordered moment, provide evidence for the Mott-insulating nature of alkaline iron selenides. From the momentum distribution of the spin spectral weight^{78,79}, it can also be observed that the damping rate in this system is smaller than that inferred for iron pnictides. The overall behaviour is similar in 234 alkaline iron selenides (for example, $Rb_{0.8}Fe_{1.6}Se_2$); however, in this system, the different vacancy pattern promotes a different AFM order⁸⁰.

Electron nematicity and its relation to magnetism.

Iron pnictides typically have parent compounds whose ground states have both a collinear $(\pi, 0)$ AFM order and a structural distortion¹⁶ (FIG. 1b). Measurements of resistivity anisotropy under uniaxial stress^{81,82} above the structural transition in 122 compounds have revealed a very large electronic nematic response; the examination of the strain dependence of the resistivity anisotropy (which is proportional to the electronic nematicity) provides compelling evidence that the structural transition is electronically driven. Other, less direct, methods for probing the nematic correlations^{83–85} have yielded results consistent with that conclusion.

One possible explanation for the electronic–nematic transition is the presence of a magnetic Ising–nematic order. It was recognized from the beginning of the FeSC field that models with quasi-local moments with frustrated Heisenberg J_1 – J_2 interactions²⁰ feature this kind of Ising–nematic transition^{50,51,67,86}, and, more recently, similar conclusions have been reached on the basis of models based on Fermi-surface instabilities⁸⁷. Although this magnetic mechanism has had considerable success as an explanation for nematicity, it is yet to be unequivocally established. An alternative interpretation attributes the origin of the nematic order to orbital ordering^{58,88–90}. Indeed, one manifestation of this ordering has been observed: ARPES measurements in

uniaxially pressurized $BaFe_{2-x}T_xAs_2$ show a splitting between the two orthogonal bands that have dominant d_{xz} and d_{yz} characters⁹¹, and which are otherwise degenerate. Adding to the complication is the fact that symmetry allows a bilinear coupling between the magnetic Ising–nematic and orbital order parameters; thus, an effort is needed to sharpen the distinction between the different scenarios.

Two recent developments are worth emphasizing. The first is the measurement of spin-excitation anisotropies by neutron scattering experiments^{92,93}. Iron pnictides exhibit collinear AFM order; applying a uniaxial strain along one axis of the orthorhombic lattice yields spin-excitation anisotropy, as measured by the difference in the spin structure factor at two wavevectors, $S[(\pi, 0), \omega] - S[(0, \pi), \omega]$. Above the structural transition temperature, T_s , experiments reveal a strong spin-excitation anisotropy in the optimally doped regime, in which the splitting between the d_{xz} and d_{yz} bands measured by ARPES is already considerably reduced. Moreover, although the orbital splitting energy measured by ARPES ranges from about 60 meV in undoped $BaFe_2As_2$ to about 20 meV near the optimal electron doping, the energy scale for the spin-excitation anisotropy remains about 60 meV for all the relevant doping levels. These results suggest that magnetism plays a dominant role in the formation of the nematic correlations⁹³.

The second development concerns bulk FeSe. This compound displays a tetragonal-to-orthorhombic structural transition with $T_s \approx 90$ K (FIG. 4d), but no Néel transition has been detected^{194–97}. It has been suggested that these results imply a failure of the magnetism-based model for the origin of the structural phase transition^{96,97}. However, there is a natural way to understand this behaviour within the magnetic picture. Several groups have studied the frustrated magnetism associated with the spin-exchange interactions among the local moments^{59,60,98}. On the basis of the theoretical phase diagram associated with the frustrated bilinear–biquadratic exchange interactions, it was proposed that the structural transition in FeSe originates from an Ising–nematic order of an antiferro-quadrupolar phase⁵⁹. In this kind of order, although the spins have a preferred axis, they do not orient along it, and so they break the spin rotational invariance while preserving the time-reversal symmetry. Although no static AFM order is realized, the collective modes of this quadrupolar state yield $(\pi, 0)$ magnetic fluctuations, which have been observed by inelastic neutron scattering measurements^{99,100}.

Quantum criticality

In many correlated-electron materials, there are several competing ground states, and it is often possible to go from one to another through a ‘quantum critical point’ (QCP) by adjusting some control parameter, for example, pressure, magnetic field or chemical composition. Dynamical fluctuations of the order parameter are important for determining the behaviour of the system in the neighbourhood of the QCP. Although quantum phase transitions between distinct ground states occur at absolute zero, their effects may be observed over a

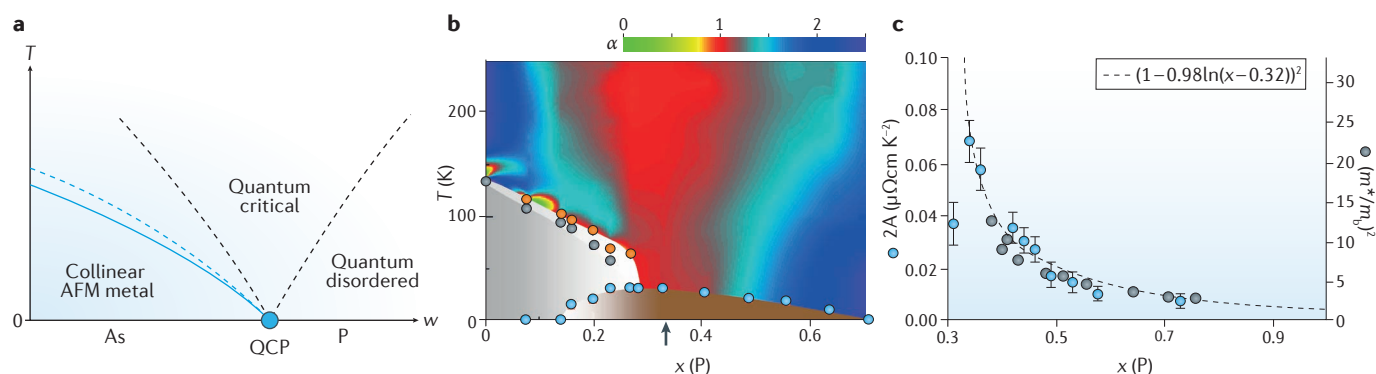


Figure 5 | Quantum criticality in iron pnictides. **a** | Quantum criticality in the theoretically proposed phase diagram for the substitution of phosphorus, P, for arsenic, As. The blue dot marks a quantum critical point (QCP). The crossovers out of the quantum criticality region are indicated by the dashed lines; the blue lines represent the thermally driven antiferromagnetic (AFM) transition (solid line) and the Ising–nematic transition (dashed line). **b** | Phase diagram of $\text{BaFe}_2(\text{As}_{1-x}\text{P})_2$. The orange, grey and blue circles represent the structural, magnetic (grey region) and superconducting (brown region) transitions, respectively. The colour shading describes the variation of the resistivity exponent α in its temperature dependence: $\rho = \rho_0 + AT^\alpha$, in which ρ_0 is the resistivity at $T = 0$ and A is a constant for a given composition. The arrow marks the QCP at the critical doping $x = x_c = 0.33$. **c** | Divergence of the effective mass m^* (normalized by the band mass m_b ; grey)¹⁰⁵ and A (blue), the T^2 coefficient of the electrical resistivity, on approaching the QCP. T , temperature; w , the order parameter. Panel **a** is adapted with permission from REF. 86, Proceedings of the National Academy of Sciences. Panel **b** is adapted with permission from REF. 18, Institute of Physics; courtesy of Matsuda. Panel **c** is from REF. 103, Nature Publishing Group.

range of non-zero temperatures. The physics of quantum criticality in iron pnictides and chalcogenides has been discussed in a recent review¹⁸.

Because iron-based superconductors exhibit several different phases in their phase diagrams (AFM, paramagnetic and superconducting), it is reasonable to expect to be able to access one or more QCPs by identifying the appropriate control parameters. FIGURE 5a shows an example in which the QCP separates an AFM metal from a paramagnetic one, and is accessed by the parameter w that was introduced earlier to measure electron correlations.

The considerations for electronic correlations and proximity to a Mott transition discussed in the previous sections imply that by tuning the ratio of kinetic energy to Coulomb repulsion from small to large it is possible to pass from an AFM state to a paramagnetic one, crossing a magnetic QCP. It was proposed that isoelectronic substitution of phosphorus for arsenic in, for example, LaFeAsO or BaFe_2As_2 would increase this ratio⁸⁶, here measured by w (FIG. 5a). This happens because phosphorus is substantially smaller than arsenic, which leads to a reduction in the unit-cell volume (as well as in the pnictogen height), thus increasing the kinetic energy.

The isoelectronic tuning of w is a convenient tool for exploring the physics of quantum criticality and for varying the effects of correlations in a straightforward way. The substitution of phosphorus for arsenic weakens correlation effects. This complements the study of the comparison between chalcogenides and pnictides: as we have seen, the former have stronger correlations than the latter.

The phase diagram proposed in FIG. 5a shows a quantum critical region, in which the thermodynamic and transport properties are expected to have a power-law dependence on the temperature and tuning parameter. The ordered phase is AFM and disappears into a

paramagnetic Fermi-liquid phase upon crossing the QCP. Crossovers out of the region of quantum criticality are denoted by the dashed black lines. The blue lines represent the thermally driven AFM transition (solid line) and an Ising–nematic transition that manifests itself through a structural transition (dashed line). The thermal transitions are represented as two split second-order transitions, but could also be concurrent first-order transitions.

The prediction of the creation of a quantum criticality through isoelectronic substitution has been experimentally confirmed; this is illustrated in FIG. 5b,c. In FIG. 5b, the colour shading represents the temperature exponent, α , in the expression for resistivity ($\rho = \rho_0 + AT^\alpha$, in which ρ_0 is the resistivity at $T = 0$ and A is a constant for a given composition) in $\text{BaFe}_2(\text{As}_{1-x}\text{P})_2$, a 122 compound, in which the QCP occurs at a critical value of $x = x_c \approx 0.33$ (REF. 101). The red area highlights the quantum critical regime in which the resistivity has a linear temperature dependence, as is characteristic for a 2D AFM QCP¹⁰². As the QCP is approached, the expected singular behaviour of thermodynamic quantities is observed¹⁰³, along with the anticipated¹⁰² logarithmic increase in the electron effective mass, m^* , as $x \rightarrow x_c$ (FIG. 5c). The left-hand scale in FIG. 5c shows the measured coefficient, A , of the T^2 resistivity in the region corresponding to ‘quantum disordered’, in which it should vary as m^{*2} (REF. 104). This figure shows consistent quantum critical behaviour in both transport and thermodynamic measurements: in this case, specific heat and de Haas–van Alphen measurements¹⁰⁵.

Isoelectronic substitution and the associated quantum criticality are of particular interest in the context of superconductivity: phosphorus substitution for arsenic in the Ba 122 compound destroys antiferromagnetism (grey region in FIG. 5b) and enables superconductivity

(brown region in FIG. 5b). Although direct access to the QCP is inhibited by the presence of superconductivity, it is observed that as x is varied, the maximum $T_c(x)$ is found very close to $x=x_c$, similarly to what is observed in other strongly correlated systems.

Quantum criticality and emergent phases beyond iso-electronic dopings. For carrier-doped iron arsenides, it remains to be established whether the effects of quantum criticality near optimal doping persist over a substantial temperature and energy range. The dopings that have been investigated include electron doping associated with cobalt or nickel substitution for iron and hole doping induced by potassium substitution for barium; these dopings have been studied by thermopower¹⁰⁶, NMR spectroscopy¹⁰⁷ and ultrasonic attenuation¹⁰⁸ measurements. Studies based on electrical transport^{109,110}, neutron scattering¹¹¹ and X-ray scattering¹¹² have revealed the evolution of the transitions towards AFM order, as well as structural order (and the implicated electronic–nematic order) in cobalt-doped BaFe_2As_2 (REF. 112). The corresponding transition temperatures T_N and T_S gradually decrease with increasing x , which suggests the presence of a QCP underneath the superconducting dome. However, the precise way in which the T_N and T_S can be extrapolated towards the zero-temperature limit as functions of doping x is still unknown¹¹³.

This issue has been systematically investigated by neutron and X-ray scattering studies of the structural and magnetic phase transitions of $\text{BaFe}_{2-x}\text{Ni}_x\text{As}_2$ (REF. 114). The results are consistent with the T_N (for the primary $(\pi, 0)$ AFM order) and the T_S evolving towards the same QCP. However, before the T_N and T_S reach zero, the transitions are interrupted by a new magnetic phase (FIG. 1b). The details of this magnetic phase are not yet clear, but it exhibits glassy characteristics¹¹⁵. Thus, the picture that has emerged from these measurements is that, when the primary magnetic order is sufficiently weakened, other emergent magnetic phases appear. In other words, the quantum criticality operates over a substantial dynamical range in the form of ‘avoided’ quantum criticality. The concurrent nature of the quantum criticality associated with the primary AFM order and the electronic nematic order appears to have the same form as that of the quantum criticality predicted for isoelectronically tuned iron pnictides⁸⁶.

Further studies are necessary to explore quantum criticality in carrier-doped iron arsenides; for example, it would be illuminating to investigate the evolution of the low-temperature electrical resistivity as a function of doping in the normal state induced by suppressing superconductivity via a strong magnetic field, as was discussed for the isoelectronic doping case¹⁰³. This should be a particularly promising approach, given that the electrical resistivity at optimal cobalt doping varies almost linearly with temperature⁸¹. Likewise, exploring the E/T scaling in the magnetic and nematic dynamics by neutron scattering would be exceedingly instructive.

We close this section by briefly commenting on alkaline iron pnictides, AFe_2As_2 with $\text{A} = \text{K}, \text{Rb}$ or Cs . In these systems, the $3d$ -electron filling N is nominally

5.5, which differs greatly from the usual cases of $N \approx 6$ (REF. 15). Even though their superconducting transition temperatures are small — 3.5 K for $\text{A} = \text{K}$ and even smaller for $\text{A} = \text{Rb}$ or Cs — experimental evidence suggests that the superconductivity is unconventional^{116–119}. Moreover, there is a huge mass enhancement, implying that these systems are strongly correlated^{120–122}. The measured Grüneisen ratio suggests an increasing proximity to quantum criticality as A goes from K through Rb to Cs ¹²². It will be illuminating to understand the nature of this QCP and its detailed relationship with superconductivity, as well as to explore the ways in which to extend N from 5.5 to 5 (REF. 122).

Unconventional superconductivity

We have seen that electron correlations in iron pnictides and chalcogenides are sufficiently strong to place these materials in the bad-metal regime and that frustrated magnetism of local moments describes the dominant part of their magnetic behaviour. We now turn to the implications for unconventional superconductivity and the structure and amplitude of the superconducting pairing.

The proximity of the superconducting phase to the AFM ordered one suggests the importance of the AFM correlations for superconductivity. Through the correlation effects implied by the bad-metal phenomenology and the data relating to the magnetic ordering and dynamics, we have emphasized the role of frustrated AFM exchange interactions. The AFM nature of such interactions favours pairing in a spin-singlet channel, which is antisymmetric in spin space. Because electrons are fermions, the overall wave function must be antisymmetric under the exchange of electrons. Consequently, the orbital part of the pairing wave function must be symmetric.

Superconducting pairing structure and amplitude.

A characteristic feature of iron pnictides and chalcogenides is that the bilinear exchange interactions contain both the nearest-neighbour interaction, J_1 , and the next-nearest-neighbour interaction, J_2 . We have emphasized the reasons why J_2 is important in the context of the microscopic physics of these materials; its importance is also supported by the agreement between the theoretical spin dynamics and those measured from neutron scattering experiments. J_2 favours an extended s -wave pairing function, with the leading term in the wave-vector dependence being $\cos(k_x)\cos(k_y)$. In relation to the tetrahedral D_{4h} point group symmetry, this pairing belongs to a pairing state with an A_{1g} symmetry.

For optimally doped iron pnictides, whose Fermi surfaces in the Brillouin zone typically consist of the hole Fermi pockets near the $\Gamma = (0, 0)$ point and of the electron Fermi pockets near the $M = (\pm\pi, 0)$ and $(0, \pm\pi)$ points, this extended s -wave gap function is non-zero everywhere on the Fermi surfaces. Moreover, it changes sign across the hole and electron pockets. These characteristics of the pairing function are reflected in the single-particle excitation spectrum at the Fermi surface. Where the pairing function is non-zero, a gap develops in the spectrum. Where the gap vanishes, the spectrum

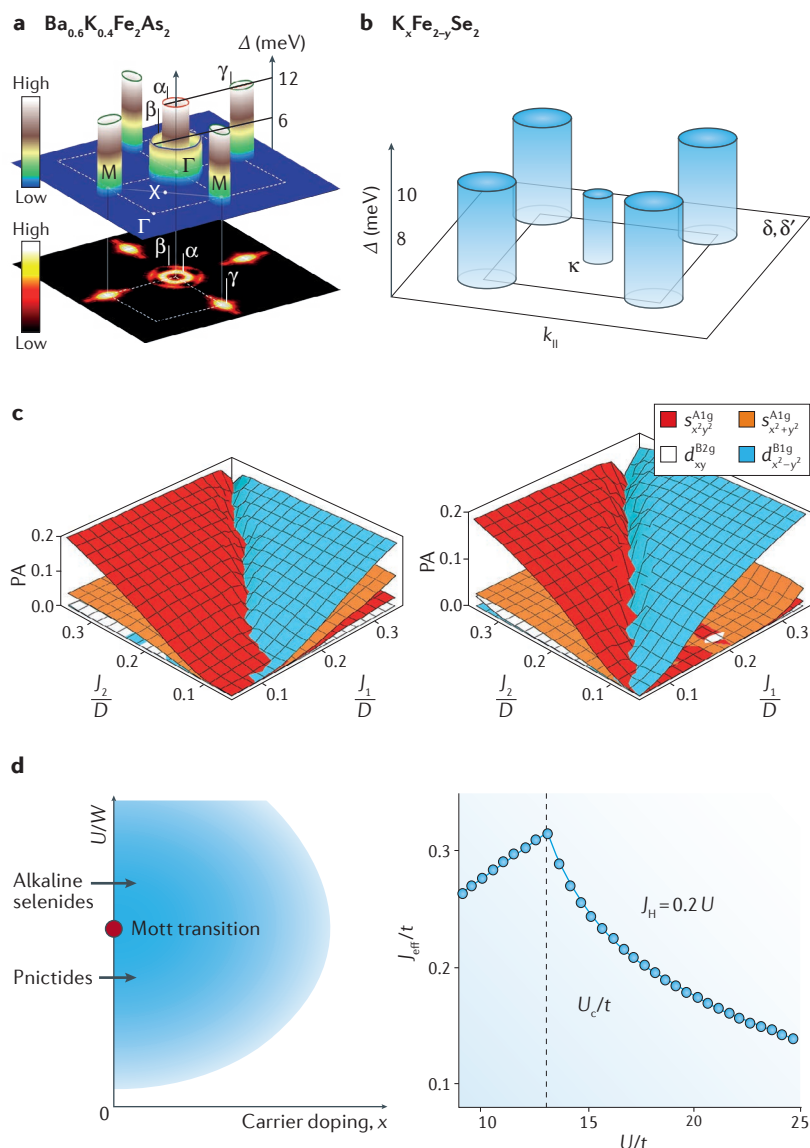


Figure 6 | Superconductivity in iron pnictides and chalcogenides. a | Size of the superconducting gap, Δ , on the hole (α and β) and electron (γ) Fermi pockets in $\text{Ba}_{0.6}\text{K}_{0.4}\text{Fe}_2\text{As}_2$. An intensity plot of the Fermi surface is shown at the bottom. Here, $\Gamma = (0,0)$ denotes the centre of the planar Brillouin zone, $M = (\pm\pi, 0)$ and $(0, \pm\pi)$ are the zone corners and X is midway between two adjacent M points. **b** | Size of Δ on the electron Fermi pockets of dominant (δ and δ') and small (κ) spectral weight in $\text{K}_x\text{Fe}_{2-y}\text{Se}_2$. Here, κ is near the zone centre Γ , δ and δ' are located close to the zone corner M and k_{\parallel} denotes the planar wavevector. **c** | Pairing amplitudes (PA) calculated for iron pnictides (left) and chalcogenides (right). Here, the four dominant pairing states are: two extended s-wave pairing states whose symmetry is A_{1g} and whose pairing functions are $\cos(k_x)\cos(k_y)$ and $\cos(k_x) + \cos(k_y)$, respectively; a d-wave state whose symmetry is B_{2g} and whose pairing function is $\sin(k_x)\sin(k_y)$; and a d-wave state whose symmetry is B_{1g} and whose pairing function is $\cos(k_x) - \cos(k_y)$. **d** | Left, schematic phase diagram near a Mott transition. The shading marks the parameter regime with strong antiferromagnetic correlations. Right, the exchange interaction, J_{eff} , plotted as a function of the Hubbard interaction, U , for a Hund's coupling $J_H = 0.2U$ in a two-orbital Hubbard model. The Mott transition is realized when U reaches the critical value U_c . D , renormalized bandwidth; J_1 and J_2 , exchange interactions between the nearest-neighbour and next-nearest-neighbour sites, respectively; t , kinetic-energy parameter; W , bare bandwidth parameter. Panel **a** is adapted with permission from REF. 123, Institute of Physics. Panel **b** is adapted with permission from REF. 134, American Physical Society. Panel **c** is from REF. 49, Nature Publishing Group. Panel **d** (left) is from REF. 49, Nature Publishing Group. Panel **d** (right) is adapted with permission from REF. 143, American Physical Society.

is 'gapless'; in other words, there is a node in the gap. A spectrum that is fully gapped has been identified from ARPES measurements. This spectrum is shown in FIG. 6a, in which the gap function, Δ , is plotted for the different parts of the Fermi surface; it has a maximum magnitude of about 10 meV. The ratio $2\Delta/T_C$ is roughly 4–7 (REF. 123) — larger than the Bardeen–Cooper–Schrieffer (BCS) value of approximately 3.5.

By contrast, when J_1 is dominant, d -wave pairing with a $\cos(k_x) - \cos(k_y)$ form factor and B_{1g} symmetry is favoured. In the magnetic frustration regime, in which J_2 and J_1 are comparable in size, a quasi-degeneracy in pairing channels emerges in model calculations. It is interesting that this situation arises from various approaches, regardless of whether the correlations are treated non-perturbatively or perturbatively^{49,53–56,124–128}.

To distinguish among these various approaches, it is instructive to compare the behaviour of the gap in iron chalcogenides, especially because there are cases in which they have only electron Fermi surfaces. This property is illustrated for the case of $\text{K}_x\text{Fe}_{2-y}\text{Se}_2$ in FIG. 6b. We note that the gap is nodeless. Moreover, the magnitude of the gap for the electron Fermi pockets that have the dominant spectral weight (those near the M points in the Brillouin zone) is comparable to that of iron pnictides. This is consistent with the fact that the T_C of $\text{K}_x\text{Fe}_{2-y}\text{Se}_2$ is comparable to that of iron pnictides.

This comparison shows that the pairing amplitudes are similarly large in systems with and without hole pockets, or, equivalently, with and without Fermi-surface nesting. This is naturally understood in models in which pairing is driven by short-range interactions, such as exchange interactions. The pairing amplitude as a function of J_1 and J_2 in multi-orbital models with pnictide- and chalcogenide-type Fermi surfaces⁴⁹ is shown in FIG. 6c. Despite their distinctive Fermi surfaces, the dominant pairing channels as a function of the exchange interactions are similar in the two cases and the pairing amplitudes are comparable.

Effects of orbital selectivity on superconducting pairing.

We have discussed how electron correlations can show strong orbital selectivity, which noticeably affects the electronic properties of the normal states. A natural question is whether the pairing symmetry and amplitudes in the superconducting states are also influenced by orbital selectivity. The study of this issue provides additional means to explore the effect of electron correlations on the properties of the superconducting state.

Within the strong-coupling approach, the pairing order parameter is defined in the orbital basis, and the orbital selectivity can lead to surprising effects. In the common case, in which the dominant pairing is in a full-gap s-wave A_{1g} channel, sufficiently strong orbital selectivity can lead to an anisotropic gap along the electron pockets and to the splitting of spin resonance peaks¹²⁹. Such effects have been observed experimentally by ARPES¹³⁰ and neutron scattering^{131,132}, respectively.

A more dramatic effect arises in the context of alkaline iron selenides. As previously discussed, in a multi-orbital J_1 – J_2 model with orbital-independent J_1 and J_2 ,

the dominant pairing symmetry is either an s -wave A_{1g} channel if J_2 is dominant or a d -wave B_{1g} channel if J_1 is dominant. A recent study¹³³ on this model with orbital-dependent J_1 and J_2 revealed that orbital selectivity plays an essential role in stabilizing an intermediate orbital-selective B_{1g} pairing state that is constructed from the conventional s -wave A_{1g} and d -wave B_{1g} states in the parameter regime in which the two are quasi-degenerate. In this orbital-selective B_{1g} pairing state, the dominant pairing amplitude is restricted to the d_{xz} and d_{yz} orbital subspace, in which the pairing state belongs to the B_{1g} representation of the associated point group, but has a form factor belonging to the A_{1g} representation, owing to its non-trivial orbital structure. It was shown that for alkaline iron chalcogenides this pairing state exhibits a full gap and can produce a spin resonance at wave vector $(\pi, \pi/2)$, which resolves a widely recognized conflict between the observations of ARPES and neutron scattering experiments^{134–139}.

Box 2 | Take-home messages

The normal state of iron-based superconductors is a bad metal

More specifically, the d.c. electrical resistivity at room temperature is large, reaching the Mott–Ioffe–Regel limit. Correspondingly, the Drude weight of the optical conductivity is strongly suppressed compared to its non-interacting counterpart. A relatively modest enhancement of the electron correlation strength through a reduction in the kinetic energy leads to a fully localized, Mott-insulating regime. These and other properties provide compelling evidence that iron pnictides and chalcogenides are strongly correlated, in the sense that the effect of electron correlations is non-perturbative. These results also suggest that the normal state is in proximity to a Mott transition. Orbital selectivity has also been found in the bad-metal regime, with its extreme form being an orbital-selective Mott phase.

The spin excitations map out a spin-wave-like spectrum

The total spectral weight of the observed excitations is large, corresponding to a local moment of the order of one to several μ_B per iron ion (μ_B is the Bohr magneton). Across the different materials, the variation in the magnitude of the local moments is correlated with the variation in the degree of electron correlations inferred from studies of electrical transport and charge dynamics. The energy dispersions of the spin excitations implicate a J_1 – J_2 magnetic frustration (with J_1 and J_2 the exchange interactions between the nearest-neighbour and next-nearest-neighbour sites, respectively), as has been theoretically recognized since the beginning of the field. The detailed energy and momentum distributions of the spin spectral weight encode the damping of the spin excitations; the variation in the spin spectral weight across the different materials also seems consistent with the corresponding variation in the degree of electron correlations.

Electronic nematicity

Electronic nematicity has been observed in the normal state of many, if not all, iron-based superconductors (FeSCs). There is considerable evidence that its origin lies in the spin degrees of freedom, although the issue remains to be fully settled.

Quantum criticality

Compelling experimental evidence has accumulated for the presence of the quantum criticality that was predicted to occur in isoelectronic phosphorus-doped iron arsenides. There are also indications of quantum criticality in carrier-doped iron arsenides, although in this case further evidence is needed.

Unconventional superconductivity

Superconductivity is unconventional in the sense that it is primarily driven by electron–electron interactions and, consequently, the superconducting pairing is not in the conventional s -wave channel. We have summarized the arguments supporting the hypothesis that superconductivity is primarily driven by antiferromagnetic correlations, and discussed the implications of the comparably large superconducting transition temperature, T_c , and pairing amplitudes observed in FeSCs with or without Fermi-surface nesting. Finally, there is a considerable theoretical basis for the quasi-degeneracy among several competing channels of superconducting pairing.

Connection between iron pnictides and iron chalcogenides. We have seen that most iron pnictides and essentially all iron chalcogenides have an electron occupancy of the $3d$ orbitals that is close to 6, and that the degree of electronic correlations is relatively weak for iron phosphides but increases for arsenides and is strong for chalcogenides. A unified phase diagram is obtained from theoretical studies on the correlation effects — of both U and J_H — in multi-orbital Hubbard models^{41,42,44}, similar to the phase diagram shown in FIG. 2d. A unified phase diagram is consistent with the fact that both iron pnictides and iron chalcogenides show bad-metal behaviour in their normal states, and it is also compatible with the results of dynamical mean-field studies in various iron pnictides and chalcogenides⁴⁸. Following these considerations, a physical pathway may be constructed to connect the insulating 245 alkaline iron selenides with their superconducting counterparts^{40,41}, providing the basis for the placement of these materials in the illustrative phase diagram shown in FIG. 6d. We also expect further progress in this direction based on materials systems in which the degree of electronic correlations, including orbital selectivity, can be continuously tuned^{140,141}.

Potential settings for optimizing superconductivity.

One challenging question in physics is whether there is a principle for the optimization of T_c . Superconductivity was initially observed in iron pnictides with nested hole and electron Fermi pockets, but we have already referred to the large number of recent experiments that show that iron chalcogenides with Fermi surfaces containing only electron pockets exhibit superconductivity of comparable strength. For example, single-layer FeSe on a SrTiO_3 substrate has only electron Fermi pockets, but it has the highest T_c of all the FeSCs. By contrast, Li(Fe,Co)As , which has almost perfectly nested Fermi pockets, is non-superconducting¹⁴². These results suggest that the geometry of the Fermi surface plays only a secondary role in superconductivity.

From a theoretical perspective, the pairing amplitudes shown in FIG. 6c for both iron pnictides and alkaline iron selenides can shed light on the issue of optimizing superconductivity. The results illustrated therein indicate that the pairing amplitudes are proportional to J/D , in which J is the AFM exchange coupling and D is the effective bandwidth renormalized by electron–electron interactions, whereas W and t in FIG. 6d are the bare bandwidth and the kinetic-energy (hopping) parameter, respectively.

This result, that the pairing amplitude increases with J/D , can be generalized to the following principle, which is illustrated in FIG. 6d (left panel): the maximum pairing amplitude and, hence, the optimal superconductivity is reached in the parameter regime corresponding to the region near the Mott transition in the phase diagram. A recent study on a multi-orbital Hubbard model that used a slave rotor approach demonstrated that the exchange interactions increase as the Mott transition is approached from both the insulating and the bad-metal sides¹⁴³ (FIG. 6d, right panel). Conversely, for a system with carrier doping, the renormalized bandwidth

D is reduced as the Mott transition is approached by decreasing doping. Correspondingly, both the ratio J/D and the superconducting pairing amplitudes are maximized at the boundary between electronic localization and delocalization. This principle suggests a route for optimizing superconductivity. It also explains some key experimental observations, such as the comparable T_c in iron pnictides and alkaline iron selenides, which have very different Fermi-surface geometries. In fact, it was demonstrated¹⁶ that these two materials have comparable exchange interactions. In addition, both systems can be considered close to a Mott transition (FIG. 6d) and, therefore, have a comparable degree of bad metallicity and renormalized bandwidth.

Conclusions

Concerted efforts over the past years have led to a wide range of iron pnictides and chalcogenides that display superconductivity. Their superconducting transition temperatures are high compared to those of conventional

superconductors, and, in the bulk and at ambient pressure, they are second only to those achieved in copper oxides. Moreover, recent experiments have shown that the T_c could be increased further in iron chalcogenides. The main findings on the microscopic physics of the iron pnictides and chalcogenides are summarized in BOX 2.

The properties observed in iron pnictides and chalcogenides and the theoretical considerations outlined in this Review suggest that optimized superconductivity is found in bad metals that are not only close to a magnetic order, but are also at the boundary between electronic localization and delocalization. This characteristic connects FeSCs to the unconventional superconductivity that has been observed in other classes of strongly correlated materials, such as copper oxides, heavy fermion metals and organic charge-transfer salts. Indeed, the normal state of all of these other superconductors satisfies the criterion for bad metals. Therefore, higher- T_c superconductivity may appear in materials that possess even larger AFM exchange interactions but retain bad metallicity.

- Kamihara, Y., Watanabe, T., Hirano, M. & Hosono, H. Iron-based layered superconductor $\text{La}[\text{O}_{1-x}\text{F}_x]\text{FeAs}$ ($x = 0.05\text{--}0.12$) with $T_c = 26\text{ K}$. *J. Am. Chem. Soc.* **130**, 3296–3297 (2008).
- Bednorz, J. G. & Müller, K. A. Possible high T_c superconductivity in the Ba–La–Cu–O system. *Z. Phys. B* **64**, 189–193 (1986).
- Ren, Z. A. *et al.* Superconductivity at 55 K in iron-based F-doped layered quaternary compound $\text{Sm}[\text{O}_{1-x}\text{F}_x]\text{FeAs}$. *Chin. Phys. Lett.* **25**, 2215–2216 (2008).
- Wang, Q.-Y. *et al.* Interface-induced high-temperature superconductivity in single unit-cell FeSe films on SrTiO_3 . *Chin. Phys. Lett.* **29**, 037402 (2012). **Observation of superconductivity in the single-layer FeSe system that possesses the highest superconducting transition temperature in FeSCs.**
- He, S. *et al.* Phase diagram and electronic indication of high-temperature superconductivity at 65 K in single-layer FeSe films. *Nat. Mater.* **12**, 605–610 (2013).
- Lee, J. J. *et al.* Interfacial mode coupling as the origin of the enhancement of T_c in FeSe films on SrTiO_3 . *Nature* **515**, 245–248 (2014).
- Zhang, Z. *et al.* Onset of the Meissner effect at 65 K in FeSe thin film grown on Nb-doped SrTiO_3 substrate. *Sci. Bull.* **60**, 1301–1304 (2015).
- Ge, J.-F. *et al.* Superconductivity above 100 K in single-layer FeSe films on doped SrTiO_3 . *Nat. Mater.* **14**, 285–289 (2015).
- Boeri, L., Dolgov, O. V. & Golubov, A. A. Is $\text{LaFeAsO}_{1-x}\text{F}_x$ an electron-phonon superconductor? *Phys. Rev. Lett.* **101**, 026403 (2008).
- Rotter, M., Tegel, M. & Johrendt, D. Superconductivity at 38 K in the iron arsenide $(\text{Ba}_{1-x}\text{K}_x)\text{Fe}_2\text{As}_2$. *Phys. Rev. Lett.* **101**, 107006 (2008).
- Hsu, F.-C. *et al.* Superconductivity in the PbO-type structure $\alpha\text{-FeSe}$. *Proc. Natl Acad. Sci. USA* **105**, 14262–14264 (2008).
- Guo, J. *et al.* Superconductivity in the iron selenide $\text{K}_x\text{Fe}_2\text{Se}_2$ ($0 \leq x \leq 1.0$). *Phys. Rev. B* **82**, 180520 (2010).
- Sun, L. *et al.* Re-emerging superconductivity at 48 kelvin in iron chalcogenides. *Nature* **483**, 67–69 (2012).
- Yi, M. *et al.* Electronic structure of the BaFe_2As_2 family of iron-pnictide superconductors. *Phys. Rev. B* **80**, 024515 (2009).
- Sato, T. *et al.* Band structure and Fermi surface of an extremely overdoped iron-based superconductor KFe_2As_2 . *Phys. Rev. Lett.* **103**, 047002 (2009).
- Dai, P. C. Antiferromagnetic order and spin dynamics in iron-based superconductors. *Rev. Mod. Phys.* **87**, 855–896 (2015).
- Hussey, N. E., Takenaka, K. & Takagi, H. Universality of the Mott–Ioffe–Regel limit in metals. *Philos. Mag.* **84**, 2847–2864 (2004).
- Abrahams, E. & Si, Q. Quantum criticality in the iron pnictides and chalcogenides. *J. Phys. Condens. Matter* **23**, 223201 (2011).
- Fawcett, E. Spin-density-wave antiferromagnetism in chromium. *Rev. Mod. Phys.* **60**, 209–283 (1988).
- Si, Q. & Abrahams, E. Strong correlations and magnetic frustration in the high T_c iron pnictides. *Phys. Rev. Lett.* **101**, 076401 (2008). **A theoretical study that emphasizes that the parent systems of the FeSCs display bad-metal behaviour and infers that their electron correlations are strong.**
- Si, Q., Abrahams, E., Dai, J. & Zhu, J.-X. Correlation effects in the iron pnictides. *New J. Phys.* **11**, 045001 (2009).
- Qazilbash, M. M. *et al.* Electronic correlations in the iron pnictides. *Nat. Phys.* **5**, 647–650 (2009). **Experimental evidence from optical conductivity that iron arsenides possess strong electron correlations.**
- Nakajima, M. *et al.* Normal-state charge dynamics in doped BaFe_2As_2 : roles of doping and necessary ingredients for superconductivity. *Sci. Rep.* **4**, 5873 (2014).
- Yi, M. *et al.* Electronic reconstruction through the structural and magnetic transitions in detwinned NaFeAs . *New J. Phys.* **14**, 073019 (2012).
- Tamai, A. *et al.* Strong electron correlations in the normal state of the iron-based $\text{FeSe}_{0.4}\text{Te}_{0.6}$ superconductor observed by angle-resolved photoemission spectroscopy. *Phys. Rev. Lett.* **104**, 097002 (2010).
- Yi, M. *et al.* Observation of temperature-induced crossover to an orbital-selective Mott phase in $\text{A}_x\text{Fe}_{2-x}\text{Se}_2$ ($\text{A} = \text{K}, \text{Rb}$) superconductors. *Phys. Rev. Lett.* **110**, 067003 (2013).
- Yi, M. *et al.* Observation of universal strong orbital-dependent correlation effects in iron chalcogenides. *Nat. Commun.* **6**, 7777 (2015). **Angle-resolved photoemission measurements provide evidence for strong and orbital-selective electron correlations in iron chalcogenides.**
- Zhu, J.-X. *et al.* Band narrowing and Mott localization in iron oxychalcogenides $\text{La}_2\text{O}_2\text{Fe}_2\text{O}(\text{Se}, \text{S})_2$. *Phys. Rev. Lett.* **104**, 216405 (2010).
- Free, D. G. & Evans, J. S. O. Low-temperature nuclear and magnetic structures of $\text{La}_2\text{O}_2\text{Fe}_2\text{OSe}_2$ from x-ray and neutron diffraction measurements. *Phys. Rev. B* **81**, 214433 (2010).
- Imada, M., Fujimori, A. & Tokura, Y. Metal-insulator transitions. *Rev. Mod. Phys.* **70**, 1039–1263 (1998).
- Freelon, B. *et al.* Mott-Kondo insulator behavior in the iron oxychalcogenides. *Phys. Rev. B* **92**, 155139 (2015).
- Fang, M.-H. *et al.* Fe-based superconductivity with $T_c = 31\text{ K}$ bordering an antiferromagnetic insulator in $(\text{Ti}, \text{K})\text{Fe}_2\text{Se}_2$. *Europhys. Lett.* **94**, 27009 (2011).
- Bao, W. *et al.* A novel large moment antiferromagnetic order in $\text{K}_{0.8}\text{Fe}_{1.6}\text{Se}_2$ superconductor. *Chin. Phys. Lett.* **28**, 086104 (2011).
- Yu, R., Zhu, J.-X. & Si, Q. Mott transition in modulated lattices and parent insulator of $(\text{K}, \text{Ti})_x\text{Fe}_2\text{Se}_2$ superconductors. *Phys. Rev. Lett.* **106**, 186401 (2011).
- Zhou, Y., Xu, D.-H., Zhang, F.-C. & Chen, W.-Q. Theory for superconductivity in $(\text{Ti}, \text{K})\text{Fe}_2\text{Se}_2$ as a doped Mott insulator. *Europhys. Lett.* **95**, 17003 (2011).
- Wang, M. *et al.* Mott localization in a pure stripe antiferromagnet $\text{Rb}_{1-x}\text{Fe}_{1.5-x}\text{S}_2$. *Phys. Rev. B* **92**, 121101 (2015).
- Wang, Z. *et al.* Orbital-selective metal–insulator transition and gap formation above T_c in superconducting $\text{Rb}_{1-x}\text{Fe}_{1.5-x}\text{Se}_2$. *Nat. Commun.* **5**, 3202 (2014).
- Ding, X., Pan, Y., Yang, H. & Wen, H.-H. Strong and nonmonotonic temperature dependence of Hall coefficient in superconducting $\text{K}_x\text{Fe}_{2-x}\text{Se}_2$ single crystals. *Phys. Rev. B* **89**, 224515 (2014).
- Li, W. *et al.* Mott behaviour in $\text{K}_x\text{Fe}_{2-x}\text{Se}_2$ superconductors studied by pump-probe spectroscopy. *Phys. Rev. B* **89**, 134515 (2014).
- Gao, P. *et al.* Role of the 245 phase in alkaline iron selenide superconductors revealed by high-pressure studies. *Phys. Rev. B* **89**, 094514 (2014).
- Yu, R. & Si, Q. Orbital-selective Mott phase in multiorbital models for alkaline iron selenides $\text{K}_{1-x}\text{Fe}_{2-x}\text{Se}_2$. *Phys. Rev. Lett.* **110**, 146402 (2013).
- Yu, R., Zhu, J.-X. & Si, Q. Orbital-dependent effects of electron correlations in microscopic models for iron-based superconductors. *Curr. Opin. Solid State Mater. Sci.* **17**, 65–71 (2013).
- Anisimov, V. I., Nekrasov, I. A., Kondakov, D. E., Rice, T. M. & Sigrist, M. Orbital-selective Mott-insulator transition in $\text{Ca}_{2-x}\text{Sr}_x\text{RuO}_4$. *Eur. Phys. J. B* **25**, 191–201 (2002).
- Yu, R. & Si, Q. $U(1)$ slave-spin theory and its application to Mott transition in a multi-orbital model for iron pnictides. *Phys. Rev. B* **86**, 085104 (2012).
- de’Medici, L., Giovannetti, G. & Capone, M. Selective Mottness as a key to iron superconductors. *Phys. Rev. Lett.* **112**, 177001 (2014).
- Bascones, E., Valenzuela, B. & Calderón, M. J. Orbital differentiation and the role of orbital ordering in the magnetic state of Fe superconductors. *Phys. Rev. B* **86**, 174508 (2012).
- Neupane, M. *et al.* Observation of a novel orbital selective Mott transition in $\text{Ca}_{1.8}\text{Sr}_{0.2}\text{RuO}_4$. *Phys. Rev. Lett.* **103**, 097001 (2009).
- Yin, Z. P., Haule, K. & Kotliar, G. Kinetic frustration and the nature of the magnetic and paramagnetic states in iron pnictides and iron chalcogenides. *Nat. Mater.* **10**, 932–935 (2011). **An article reporting calculations using dynamical mean field theory, illustrating that iron pnictides and chalcogenides provide a continuous range in the strength of electron correlations among the FeSCs.**

49. Yu, R., Goswami, P., Si, Q., Nikolic, P. & Zhu, J.-X. Superconductivity at the border of electron localization and itinerancy. *Nat. Commun.* **4**, 2783 (2013).
50. Fang, C., Yao, H., Tsai, W.-F., Hu, J. P. & Kivelson, S. A. Theory of electron nematic order in LaFeAsO. *Phys. Rev. B* **77**, 224509 (2008).
51. Xu, C., Müller, M. & Sachdev, S. Ising and spin orders in the iron-based superconductors. *Phys. Rev. B* **78**, 020501(R) (2008).
52. Laad, M. S., Craco, L., Leoni, S. & Rosner, H. Electrodynamic response of incoherent metals: normal phase of iron pnictides. *Phys. Rev. B* **79**, 024515 (2009).
53. Seo, K., Bernevig, B. A. & Hu, J. Pairing symmetry in a two-orbital exchange coupling model of oxypnictides. *Phys. Rev. Lett.* **101**, 206404 (2008).
54. Moreo, A., Daghofer, M., Riera, J. A. & Dagotto, E. Properties of a two-orbital model for oxypnictide superconductors: magnetic order, B_{2g} spin-singlet pairing channel, and its nodal structure. *Phys. Rev. B* **79**, 134502 (2009).
55. Chen, W.-Q., Yang, K.-Y., Zhou, Y. & Zhang, F.-C. Strong coupling theory for superconducting iron pnictides. *Phys. Rev. Lett.* **102**, 047006 (2009).
56. Yang, F., Wang, F. & Lee, D.-H. Fermiology, orbital order, orbital fluctuations, and Cooper pairing in iron-based superconductors. *Phys. Rev. B* **88**, 100504(R) (2013).
57. Berg, E., Kivelson, S. A. & Scalapino, D. J. A twisted ladder: relating the Fe superconductors to the high- T_c cuprates. *New J. Phys.* **11**, 085007 (2009).
58. Lv, W., Krüger, F. & Phillips, P. Orbital ordering and unfrustrated $(\pi, 0)$ magnetism from degenerate double exchange in the iron pnictides. *Phys. Rev. B* **82**, 045125 (2010).
59. Yu, R. & Si, Q. Antiferroquadrupolar and Ising-nematic orders of a frustrated bilinear-biquadratic Heisenberg model and implications for the magnetism of FeSe. *Phys. Rev. Lett.* **115**, 116401 (2015).
60. Wang, F., Kivelson, S. A. & Lee, D.-H. Nematicity and quantum paramagnetism in FeSe. *Nat. Phys.* **11**, 959–963 (2015).
61. de la Cruz, C. *et al.* Magnetic order close to superconductivity in the iron-based layered La(O_{1-x}F_x)FeAs systems. *Nature* **453**, 899–902 (2008).
Neutron scattering measurements demonstrate AFM and structural phase transitions in a parent compound of the FeSCs.
62. Diallo, S. O. *et al.* Paramagnetic spin correlations in CaFe₂As₂ single crystals. *Phys. Rev. B* **81**, 214407 (2010).
63. Harriger, L. W. *et al.* Nematic spin fluid in the tetragonal phase of BaFe₂As₂. *Phys. Rev. B* **84**, 054544 (2011).
64. Ewings, R. A. *et al.* Itinerant spin excitations in SrFe₂As₂ measured by inelastic neutron scattering. *Phys. Rev. B* **83**, 214519 (2011).
65. Yildirim, T. Origin of the 150-K anomaly in LaFeAsO: competing antiferromagnetic interactions, frustration, and a structural phase transition. *Phys. Rev. Lett.* **101**, 057010 (2008).
66. Ma, F., Lu, Z.-Y. & Xiang, T. Antiferromagnetic superexchange interactions in LaOFeAs. *Phys. Rev. B* **78**, 224517 (2008).
67. Chandra, P., Coleman, P. & Larkin, A. I. Ising transition in frustrated Heisenberg models. *Phys. Rev. Lett.* **64**, 88–91 (1990).
68. Fazekas, P. *Lecture Notes on Electron Correlation and Magnetism* Ch. 5 (World Scientific, 1999).
69. Yu, R. *et al.* Spin dynamics of a J_1 – J_2 – K model for the paramagnetic phase of iron pnictides. *Phys. Rev. B* **86**, 085148 (2012).
70. Wysocki, A. L., Belashchenko, K. D. & Antropov, V. P. Consistent model of magnetism in ferropnictides. *Nat. Phys.* **7**, 485–489 (2011).
71. Liu, M. S. *et al.* Nature of magnetic excitations in superconducting BaFe_{1.9}Ni_{0.1}As₂. *Nat. Phys.* **8**, 376–381 (2012).
Inelastic neutron scattering measurements demonstrate that the integrated spin spectral weight of iron pnictides is much larger than what is expected from particle–hole excitations near the Fermi energy.
72. Dong, J. *et al.* Competing orders and spin-density-wave instability in La(O_{1-x}F_x)FeAs. *Europhys. Lett.* **83**, 27006 (2008).
73. Knolle, J., Eremin, I. & Moessner, R. Multiorbital spin susceptibility in a magnetically ordered state: orbital versus excitonic spin density wave scenario. *Phys. Rev. B* **83**, 224503 (2011).
74. Ma, F., Ji, W., Hu, J., Lu, Z.-Y. & Xiang, T. First-principles calculations of the electronic structure of tetragonal α -FeTe and α -FeSe crystals: evidence for a bicollinear antiferromagnetic order. *Phys. Rev. Lett.* **102**, 177003 (2009).
75. Wen, J. Magnetic neutron scattering studies on the Fe-based superconductor system Fe_{1-x}Te_{1-x}Se_x. *Ann. Phys.* **358**, 92–107 (2015).
76. Yu, R., Goswami, P. & Si, Q. The magnetic phase diagram of an extended J_1 – J_2 model on a modulated square lattice and its implications for the antiferromagnetic phase of K_{0.8}Fe_{1.2}Se₂. *Phys. Rev. B* **84**, 094451 (2011).
77. Cao, C. & Dai, J. Block spin ground state and three-dimensionality of (K, Ti)Fe_{1-x}Se₂. *Phys. Rev. Lett.* **107**, 056401 (2011).
78. Wang, M. *et al.* Spin waves and magnetic exchange interactions in insulating Rb_{0.89}Fe_{1.58}Se₂. *Nat. Commun.* **2**, 580 (2011).
79. Chi, S. *et al.* Neutron scattering study of spin dynamics in superconducting (Ti, Rb)₂Fe₂Se₅. *Phys. Rev. B* **87**, 100501 (2013).
80. Wang, M. *et al.* Two spatially separated phases in semiconducting Rb_{0.8}Fe_{1.2}S₂. *Phys. Rev. B* **90**, 125148 (2014).
81. Chu, J. H., Kuo, H.-H., Analytis, J. G. & Fisher, I. R. Divergent nematic susceptibility in an iron arsenide superconductor. *Science* **337**, 710–712 (2012).
An experimental study of resistivity anisotropy in the presence of an uniaxial strain, demonstrating that the structural transition is driven by electronic nematicity.
82. Kuo, H.-H., Chu, J.-H., Kivelson, S. A. & Fisher, I. R. Ubiquitous signatures of nematic quantum criticality in optimally doped Fe-based superconductors. Preprint at <http://arXiv.org/abs/1503.00402> (2015).
83. Böhrner, A. E. *et al.* Nematic susceptibility of hole-doped and electron-doped BaFe₂As₂ iron-based superconductors from shear modulus measurements. *Phys. Rev. Lett.* **112**, 047001 (2015).
84. Thorsmølle, V. K. *et al.* Critical quadrupole fluctuations and collective modes in iron pnictide superconductors. *Phys. Rev. B* **93**, 054515 (2016).
85. Kretzschmar, F. *et al.* Nematic fluctuations and the magneto-structural phase transition in Ba(Fe_{1-x}Co_x)As₂. Preprint at <http://arXiv.org/abs/1507.06116> (2015).
86. Dai, J., Si, Q., Zhu, J.-X. & Abrahams, E. Iron pnictides as a new setting for quantum criticality. *Proc. Natl Acad. Sci. USA* **106**, 4118–4121 (2009).
Theoretical proposal for quantum criticality in iron pnictides and for its realization by isoelectronic phosphorus for arsenic substitution in iron arsenides.
87. Fernandes, R. M., Chubukov, A. V. & Schmalien, J. What drives nematic order in iron-based superconductors? *Nat. Phys.* **10**, 97–104 (2014).
88. Chen, C.-C. *et al.* Orbital order and spontaneous orthorhombicity in iron pnictides. *Phys. Rev. B* **82**, 100504(R) (2010).
89. Lee, C. C., Yin, W. G. & Ku, W. Ferro-orbital order and strong magnetic anisotropy in the parent compounds of iron-pnictide superconductors. *Phys. Rev. Lett.* **103**, 267001 (2009).
90. Krüger, F., Kumar, S., Zaanen, J. & van den Brink, J. Spin-orbital frustrations and anomalous metallic state in iron-pnictide superconductors. *Phys. Rev. B* **79**, 054504 (2009).
91. Yi, M. *et al.* Symmetry-breaking orbital anisotropy on detwinned Ba(Fe_{1-x}Co_x)As₂ above the spin density wave transition. *Proc. Natl Acad. Sci. USA* **108**, 6878–6883 (2011).
92. Lu, X. *et al.* Nematic spin correlations in the tetragonal state of uniaxial strained BaFe_{2-x}Ni_xAs₂. *Science* **345**, 657–660 (2014).
93. Song, Y. *et al.* Energy dependence of the spin excitation anisotropy in uniaxial-strained BaFe_{1.9}Ni_{0.1}As₂. *Phys. Rev. B* **92**, 180504(R) (2015).
94. McQueen, T. M. *et al.* Tetragonal-to-orthorhombic structural phase transition at 90 K in the superconductor Fe_{1.0}Se. *Phys. Rev. Lett.* **103**, 057002 (2009).
95. Medvedev, S. *et al.* Electronic and magnetic phase diagram of β -Fe₁₋₀₁Se with superconductivity at 36.7 K under pressure. *Nat. Mater.* **8**, 630–633 (2009).
96. Böhrner, A. E. *et al.* Origin of the tetragonal-to-orthorhombic phase transition in FeSe: a combined thermodynamic and NMR study of nematicity. *Phys. Rev. Lett.* **114**, 027001 (2015).
97. Baek, S.-H. *et al.* Orbital-driven nematicity in FeSe. *Nat. Mater.* **14**, 210–214 (2015).
98. Glasbrenner, J. K. *et al.* Effect of magnetic frustration on nematicity and superconductivity in iron chalcogenides. *Nat. Phys.* **11**, 953–958 (2015).
99. Rahn, M. C., Ewings, R. A., Sedlmaier, S. J., Clarke, S. J. & Boothroyd, A. T. Strong $(\pi, 0)$ spin fluctuations in β -FeSe observed by neutron spectroscopy. *Phys. Rev. B* **91**, 180501(R) (2015).
100. Wang, Q. *et al.* Strong interplay between stripe spin fluctuations, nematicity and superconductivity in FeSe. *Nat. Mater.* **15**, 159–163 (2016).
101. Kasahara, S. *et al.* Evolution from non-Fermi- to Fermi-liquid transport via isovalent doping in BaFe₂(As_{1-x}P_x)₂ superconductors. *Phys. Rev. B* **81**, 184519 (2010).
An experimental study that demonstrates the proposed quantum criticality in phosphorus-doped iron arsenides.
102. Löhneysen, H. v., Rosch, A., Vojta, M., & Wölfle, P. Fermi-liquid instabilities at magnetic quantum phase transitions. *Rev. Mod. Phys.* **79**, 1015–1075 (2007).
103. Analytis, J. G. *et al.* Transport near a quantum critical point in BaFe₂(As_{1-x}P_x)₂. *Nat. Phys.* **10**, 194–197 (2014).
104. Kadowaki, K. & Woods, S. B. Universal relationship of the resistivity and specific heat in heavy-Fermion compounds. *Solid State Commun.* **58**, 507–509 (1986).
105. Walmsley, P. *et al.* Quasiparticle mass enhancement close to the quantum critical point in BaFe₂(As_{1-x}P_x)₂. *Phys. Rev. Lett.* **110**, 257002 (2013).
106. Gooch, M., Lv, B., Lorenz, B., Guloy, A. M. & Chu, C.-W. Evidence of quantum criticality in the phase diagram of K_{0.8}Sr_{1.2}Fe₂As₂ from measurements of transport and thermoelectricity. *Phys. Rev. B* **79**, 104504 (2009).
107. Ning, F. L. *et al.* Contrasting spin dynamics between underdoped and overdoped Ba(Fe_{1-x}Co_x)As₂. *Phys. Rev. Lett.* **104**, 037001 (2010).
108. Yoshizawa, M. *et al.* Structural quantum criticality and superconductivity in iron-based superconductor Ba(Fe_{1-x}Co_x)As₂. *J. Phys. Soc. Jpn* **81**, 024604 (2012).
109. Ni, N. *et al.* Effects of Co substitution on thermodynamic and transport properties and anisotropic H_{c2} in Ba(Fe_{1-x}Co_x)As₂ single crystals. *Phys. Rev. B* **78**, 214515 (2008).
110. Chu, J.-H., Analytis, J. G., Kucharczyk, C. & Fisher, I. R. Determination of the phase diagram of the electron-doped superconductor Ba(Fe_{1-x}Co_x)As₂. *Phys. Rev. B* **79**, 014506 (2009).
111. Lester, C. *et al.* Neutron scattering study of the interplay between structure and magnetism in Ba(Fe_{1-x}Cox)₂As₂. *Phys. Rev. B* **79**, 144523 (2009).
112. Nandi, S. *et al.* Anomalous suppression of the orthorhombic lattice distortion in superconducting Ba(Fe_{1-x}Co_x)As₂ single crystals. *Phys. Rev. Lett.* **104**, 057006 (2010).
113. Zhou, R. *et al.* Quantum criticality in electron-doped BaFe_{2-x}Ni_xAs₂. *Nat. Commun.* **4**, 2265 (2013).
114. Lu, X. *et al.* Avoided quantum criticality and magnetoelastic coupling in BaFe_{2-x}Ni_xAs₂. *Phys. Rev. Lett.* **110**, 257001 (2013).
115. Lu, X. *et al.* Short-range cluster spin glass near optimal superconductivity in BaFe_{2-x}Ni_xAs₂. *Phys. Rev. B* **90**, 024509 (2014).
116. Reid, J.-Ph. *et al.* Universal heat conduction in the iron arsenide superconductor KFe₂As₂: evidence of a d -wave state. *Phys. Rev. Lett.* **109**, 087001 (2012).
117. Okazaki, K. *et al.* Octet-line node structure of superconducting order parameter in KFe₂As₂. *Science* **337**, 1314–1317 (2012).
118. Hong, X. C. *et al.* Nodal gap in iron-based superconductor CsFe₂As₂ probed by quasiparticle heat transport. *Phys. Rev. B* **87**, 144502 (2013).
119. Zhang, Z. *et al.* Heat transport in RbFe₂As₂ single crystals: evidence for nodal superconducting gap. *Phys. Rev. B* **91**, 024502 (2015).
120. Hardy, F. *et al.* Evidence of strong correlations and coherence–incoherence crossover in the iron pnictide superconductor KFe₂As₂. *Phys. Rev. Lett.* **111**, 027002 (2013).
121. Wang, A. F. *et al.* Calorimetric study of single-crystal CsFe₂As₂. *Phys. Rev. B* **87**, 214509 (2013).
122. Eilers, F. *et al.* Quantum criticality in AFe₂As₂ with A = K, Rb, and Cs suppresses superconductivity. Preprint at <http://arXiv.org/abs/1510.01857> (2015).
123. Ding, H. *et al.* Observation of Fermi-surface-dependent nodeless superconducting gaps in Ba_{0.8}K_{0.2}Fe₂As₂. *Europhys. Lett.* **83**, 47001 (2008).
Measurement of the quasi-particle excitation energy gap, which provides evidence that the superconducting pairing function in iron arsenides has no nodes.

124. Hirschfeld, P. J., Korshunov, M. M. & Mazin, I. I. Gap symmetry and structure of Fe-based superconductors. *Rep. Prog. Phys.* **74**, 124508 (2011).
 125. Goswami, P., Nikolic, P. & Si, Q. Superconductivity in multi-orbital t - J_1 - J_2 model and its implications for iron pnictides. *Europhys. Lett.* **91**, 37006 (2010).
 126. Graser, S., Maier, T. A., Hirschfeld, P. J. & Scalapino, D. J. Near-degeneracy of several pairing channels in multiorbital models for the Fe pnictides. *New J. Phys.* **11**, 025016 (2009).
 127. Kuroki, K. *et al.* Unconventional pairing originating from the disconnected Fermi surfaces of superconducting $\text{LaFeAsO}_{1-x}\text{F}_x$. *Phys. Rev. Lett.* **101**, 087004 (2008).
 128. Wang, F., Zhai, H., Ran, Y., Vishwanath, A. & Lee, D.-H. Functional renormalization-group study of the pairing symmetry and pairing mechanism of the FeAs-based high-temperature superconductor. *Phys. Rev. Lett.* **102**, 047005 (2009).
 129. Yu, R., Zhu, J.-X. & Si, Q. Orbital-selective superconductivity, gap anisotropy, and spin resonance excitations in a multiorbital t - J_1 - J_2 model for iron pnictides. *Phys. Rev. B* **89**, 024509 (2014).
 130. Ge, Q. *et al.* Anisotropic but nodeless superconducting gap in the presence of spin-density wave in iron-pnictide superconductor $\text{NaFe}_{1-x}\text{Co}_x\text{As}$. *Phys. Rev. X* **3**, 011020 (2013).
 131. Zhang, C. *et al.* Double spin resonances and gap anisotropy in superconducting underdoped $\text{NaFe}_{0.985}\text{Co}_{0.015}\text{As}$. *Phys. Rev. Lett.* **111**, 207002 (2013).
 132. Zhang, C. *et al.* Neutron spin resonance as a probe of superconducting gap anisotropy in partially detwinned electron underdoped $\text{NaFe}_{0.985}\text{Co}_{0.015}\text{As}$. *Phys. Rev. B* **91**, 104520 (2015).
 133. Nica, E., Yu, R. & Si, Q. Orbital selectivity and emergent superconducting state from quasi-degenerate s - and d -wave pairing channels in iron-based superconductors. Preprint at <http://arXiv.org/abs/1505.04170> (2015).
 134. Xu, M. *et al.* Evidence for an s -wave superconducting gap in $\text{K}_x\text{Fe}_{2-x}\text{Se}_2$ from angle-resolved photoemission. *Phys. Rev. B* **85**, 220504 (2012).
 135. Mou, D. *et al.* Distinct Fermi surface topology and nodeless superconducting gap in a $(\text{Ti}_{0.58}\text{Rb}_{0.42})\text{Fe}_{1.72}\text{Se}_2$ superconductor. *Phys. Rev. Lett.* **106**, 107001 (2011).
- An angle-resolved photoemission experiment confirming that the superconducting pairing amplitude in iron chalcogenides without Fermi-surface nesting is comparable to that in iron pnictides.**
136. Wang, X. P. *et al.* Strong nodeless pairing on separate electron Fermi surface sheets in $(\text{Ti}, \text{K})\text{Fe}_{1.78}\text{Se}_2$ probed by ARPES. *Europhys. Lett.* **93**, 57001 (2011).
 137. Wang, X.-P. *et al.* Observation of an isotropic superconducting gap at the Brillouin zone centre of $\text{Ti}_{0.63}\text{K}_{0.37}\text{Fe}_{1.78}\text{Se}_2$. *Europhys. Lett.* **99**, 67001 (2012).
 138. Park, J. T. *et al.* Magnetic resonant mode in the low-energy spin-excitation spectrum of superconducting $\text{Rb}_2\text{Fe}_2\text{Se}_5$ single crystals. *Phys. Rev. Lett.* **107**, 177005 (2011).
 139. Friemel, G. *et al.* Reciprocal-space structure and dispersion of the magnetic resonant mode in the superconducting phase of $\text{Rb}_2\text{Fe}_{2-x}\text{Se}_5$ single crystals. *Phys. Rev. B* **85**, 140511(R) (2012).
 140. Niu, X. H. *et al.* A unifying phase diagram with correlation-driven superconductor-to-insulator transition for the 122* series of iron chalcogenides. *Phys. Rev. B* **93**, 054516 (2016).
 141. Yi, M. *et al.* Electron correlation-tuned superconductivity in $\text{Rb}_{0.8}\text{Fe}_2(\text{Se}_{1-x}\text{S}_x)_2$. *Phys. Rev. Lett.* **115**, 256403 (2015).
 142. Miao, H. *et al.* Observation of strong electron pairing on bands without Fermi surfaces in $\text{LiFe}_{1-x}\text{Co}_x\text{As}$. *Nat. Commun.* **6**, 6056 (2015).
 143. Ding, W., Yu, R., Si, Q. & Abrahams, E. Effective exchange interactions for bad metals and implications for iron-based superconductors. Preprint at <http://arXiv.org/abs/1410.8118> (2014).
 144. van Delft, D. & Kes, P. The discovery of superconductivity. *Phys. Today* **63**, 38–43 (2010).
 145. Bardeen, J., Cooper, L. & Schrieffer, J. R. Microscopic theory of superconductivity. *Phys. Rev.* **106**, 162–164 (1957).
 146. Hosono, H. & Kuroki, K. Iron-based superconductors: current status of materials and pairing mechanism. *Physica C* **514**, 399–422 (2015).
 147. Si, Q. Iron pnictide superconductors: electrons on the verge. *Nat. Phys.* **5**, 629–630 (2009).
 148. Terashima, T. *et al.* Pressure-induced antiferromagnetic transition and phase diagram in FeSe . *J. Phys. Soc. Jpn* **84**, 063701 (2015).
 149. Bende, M. *et al.* Coexistence of superconductivity and magnetism in FeSe_{1-x} under pressure. *Phys. Rev. B* **85**, 064517 (2012).

Acknowledgements

The authors thank J. Analytis, M. Bende, P. C. Dai, W. Ding, L. Harriger, X. Lu and P. Nikolic for their input. They have benefited from collaborations and/or discussions with J. Dai, P. C. Dai, W. Ding, P. Goswami, K. Grube, D. H. Lu, A. H. Nevidomskyy, E. Nica, P. Nikolic, Z.-X. Shen, H. von Löhneysen, Z. Wang, M. Yi, and J.-X. Zhu. This work was supported in part by the NSF (grant number DMR-1309531) and the Robert A. Welch Foundation (grant number C-1411) (Q.S.), and by the National Science Foundation of China (grant number 11374361) and the Fundamental Research Funds for the Central Universities and the Research Funds of Renmin University of China (R.Y.). They acknowledge the support provided in part by the NSF (grant number NSF PHY11-25915) at KITP, UCSB, for our participation in the autumn 2014 programme on "Magnetism, Bad Metals and Superconductivity: Iron Pnictides and Beyond". Q.S. and E.A. acknowledge the hospitality of the Aspen Center for Physics (NSF grant number 1066293).

Competing interests statement

The authors declare no competing interests.